ADVANCES IN SOLUTION-SHEARED $MAPbI_3$ THIN FILMS THROUGH MIXED-SOLVENT ENGINEERING

by

Benjamin Smith

Submitted in partial fulfilment of the requirements for the degree of

Masters of Applied Science

at

Dalhousie University

Halifax, Nova Scotia

April 2024

Dalhousie University is located in Mi'kma'ki, the ancestral and unceded territory of the Mi'kmaq. We are all Treaty people.

DEDICATION PAGE

I dedicate this thesis to my ever-supportive friends, family, and fellow researchers.

TABLE OF CONTENTS

LIST OF TABLES

LIST OF FIGURES

ABSTRACT

The aim of this work is to produce perovskite semiconductor thin films with desirable photoactivity under high temperature deposition conditions by combining the solution shearing technique and solvent engineering. Currently, solution shearing is used to create perovskite solar cells by exploring low temperature solvents,[1] and the wettability of the blade[2]. Herein, this work reports on the role of solvent engineering in the crystallization process of solution sheared textured $MAPbI_3$ films formed at higher than 150°C temperatures and in less than 2 minutes time. Dimethyl sulfoxide (DMSO), γ-butyrolactone (GBL), and 1-methyl-2-pyrrolidinone (NMP) are examined as well as their binary combinations to prepare solution-sheared crystalline methylammonium lead iodide ($MAPbI_3$) perovskite films at temperatures higher than 150 °C, and close to the respective boiling points of the solvents. X-ray diffraction, grazing-incidence wide-angle X-ray scattering imaging, and photoluminescence (PL) were used as characterization methods to evaluate crystal size, quality, and ordering, and determine the viability of the films as optoelectronic devices. The main application explored is a perovskite solar cell, and the semiconductor's stability within the device is tested. Excellent macroscopic crystals, over 1 mm in length, are achieved using a solvent mixture containing equal volumes of DMSO and NMP. These superior 3D $MAPbI_3$ films retain their solvent–perovskite intermediate phases and exhibit high crystalline ordering, hence are essential for high-performing and stable optoelectronic devices.

LIST OF ABBREVIATIONS USED

• 2D	Two Dimensional
• 3D	Three Dimensional
• $CaTiO_3$	Calcium titanate
• CB	Chlorobenzene
• CB	Conduction Band
• CFI	Canada Foundation for Innovation
• $CH_3NH_3PbI_3$ or $MAPbI_3$	Methylammonium Lead Iodide
• CIHR	Canadian Institute of Health Research
• DMF	N,N-Dimethylformamide
• DMSO	Dimethyl sulfoxide
• ETL	Electron Transport Layer
• FA	Formamidinium
• GBL	Gamma-butyrolactone
• GIWAXS	Grazing Incidence Wide Angle X-ray Scattering
• HTL	Hole Transport Layer
• IPA	Isopropyl alcohol
• ITO	Indium Tin Oxide
• LED	Light Emitting Diode
• MA	Methylammonium
• MACl	Methylammonium chloride
• MAI	Methylammonium Iodide
• NMP	N-Methylpyrrolidone
• NRC	National Research Council
• NSERC	Natural Sciences and Engineering Research Council
• PBI_2	Lead Iodide
• PSC	Perovskite Solar Cell
• VB	Valance Band
• XRD	X-ray Diffraction

ACKNOWLEDGEMENTS

The author acknowledges financial support from the Pengrowth Energy Innovation Grant and The Bruce and Dorothy Rosetti Engineering Research Scholarship. I would like to thank my supervisor Ghada Koleilat for her constant support, as well as Sean Hinds, and my committee members Kevin Plucknett and Stanislav Sokolenko for additional support and guidance. I would like to thank my fellow students Ghada Abdelmageed for assistance in solar cell manufacturing and testing, Rania Elsebai for help in thin film preparation, and Rashad Kahwagi for encouragement and motivation in writing this thesis. Thanks to fellow students Sean Thornton and Chang-Yong Kim for their assistance in collection and analysis of Grazing Incidence Wide Angle X-ray Scattering data.

Part of the research described in this article was performed at Canadian Light Source, a national research facility of the University of Saskatchewan, which is supported by the Canada Foundation for Innovation (CFI), the Natural Sciences and Engineering Research Council (NSERC), the National Research Council (NRC), the Canadian Institutes of Health Research (CIHR), the Government of Saskatchewan, and the University of Saskatchewan.

The author thanks Pat Scallion at the FIB-SEM Facility in Mechanical Engineering at Dalhousie University for her help in microscope and XRD operation as well as data collection. The author would also like to acknowledge the support of Stephen Kuzak, Dean Grijm, Paula Colicchio, Julie O'Grady, Randy O'Shea, Paige Cameron in completing this project.

CHAPTER 1 INTRODUCTION

1.1 MOTIVATION

Perovskite research has been of great interest to those in the Koleilat research group due to the material's promising characteristics for optoelectronic applications, the variety in possible processing methods, and the interesting challenges that are faced when working with this material.

1.1.1 Metal Halide Perovskites

Metal halide perovskites have achieved impressive device performances in a short period of focused research. Today, the efficiency of 3D metal halide perovskite solar power is directly competitive with conventional silicon technology. Perovskite materials are used in devices like solar cells,[3,4] photodetectors,[5,6] phototransistors,[7,8] and LEDs[9,10].

Metal halide perovskites have attracted attention due to their photoelectric properties such as light absorption, tunable bandgaps, carrier mobility and lifetimes, as well as benefits from their ability to be solution processed[11–13]. These benefits include the potential for low processing costs, and scalable manufacturing. However, for perovskites to compete with silicon, they must overcome two key challenges: (1) their environmental stability while (2) achieving low-cost scalable manufacturing[14,15].

1.1.2 Perovskite Processing

The optical and electrical properties that make perovskite desirable for use in semiconductor devices are directly impacted by the way the material is processed. Changes in the solution processing methods from solution composition to deposition can all impact the properties of the final product. Although this complicates the scalable manufacturing of perovskites it also provides the opportunity to tune the performance of the perovskite devices through methods such as solvent engineering and tuning deposition conditions. For

example, the chemical composition and deposition of perovskite films intended for LED use may be very different from a film for solar cell use. This makes the research space for this material rather large as there will likely not be one best way to produce perovskite materials.

The promise of perovskite's low manufacturing costs comes from comparing the required processing conditions to the traditional semiconductor material of silicon. Metal halide perovskite films can be deposited from solution at lower temperatures (< 200 °C) than those used in traditional silicon production (~1000 °C). Perovskite production can also be done at a greater speed and without the use of large vacuum chambers. This allows for cost-effective manufacturing and solvent engineering to control the crystallization process within their films that drive observed electrical and optical properties[16–18].

1.1.3 Problems and Solutions

While perovskite technologies have many promising attributes it is important to recognize that the developing field has hurdles to overcome. Examples of these hurdles include toxicity, lifetime, and scalability.

Toxicity

The composition of the perovskite used in this research is discussed later in chapter 2 where it will be shown that a primary ingredient is lead. There are potentially harmful chemicals, like organic solvents used in the processing of perovskite as well as toxic lead-containing material, which persist in the finished product. How to safely deal with these chemicals in both processing and device end of life should be a concern for those that would bring perovskite to market. There is ongoing research into lead free perovskite compositions that utilize tin, as well as assessing the health effects of different solvents that can be used in perovskite production[19].

Lifetime

With exposure to a combination of light, moisture and air, perovskite films typically begin to degrade and cease to function as a semiconductor. This provides challenges during the creation of perovskite devices and the lifetime of those devices. This issue can be combated by encapsulating devices to prevent the ingress of air and moisture, but researchers are also exploring surface passivation and the inclusion of organic molecules into perovskites which have the ability to repair themselves, resulting in what is called self-healing perovskites [20,21].

Scalability

Some of the best perovskite research devices are made using perovskite films produced from spin coating[22]. This method scales up poorly and alternative, more scalable methods are discussed in section 2.2. Each method presents unique challenges and benefits as the deposition can affect the crystallization of perovskite. This means the results of research done using one method may not be directly applicable to another, and promising results from small lab scale experiments may require significant work to scale up.

There is still a lot that is unknown about the production of perovskite semiconductors, with different chemistries and processing conditions resulting in perovskite crystals of different qualities and capabilities.

1.2 THESIS STATEMENT

The use of high temperature solvent mixtures in perovskite precursor solutions has the capacity to improve their electrical performance through alterations in film morphology produced by scalable manufacturing techniques.

1.3 ORGANIZATION

Chapter 2 will provide a basic introduction to perovskite as a semiconductor material, how it can be solution processed and deposited as a thin film and used in a device. Fundamentals of electrical properties and solar cell construction are reviewed here to clarify the purpose of testing methods used and to highlight differences between perovskite and more traditional semiconductors like silicon.
Chapter 3 will cover the methods used to prepare and analyze perovskite films and devices. This includes the preparation of perovskite precursor solutions and the parameters of shearing as well as the parameters used in analysis methods with justification for the choice of these methods.

Chapter 4 will discuss the results of this experimentation, highlighting the differences between the morphologies and the varying light reactivity between films made using different solvents and solvent mixtures. This chapter also shows a solar cell device made from the most promising mixture and the stability of that device.
Chapter 5 provides concluding remarks on the work along with recommendations for potential future work.

1.4 CONTRIBUTIONS

The contributions to the research in this thesis are as follows. Grazing-incidence wide-angle scattering data collections and analysis was performed but Sean T. Thornton, Vlad Chiriac, and Chang-Yong Kim. Thin film production was performed by Benjamin T. Smith, with assistance from Rania Elsebai and Rashad F. Kahwagi. Absorbance data collection and solar cell fabrication was done by Benjamin T. Smith with assistance from Ghada Abdelmageed. All other work was performed by Benjamin T. Smith

CHAPTER 2 BACKGROUND

This chapter gives background information on the crystal structure of perovskites and the processing techniques that are used to grow crystals of this structure deposited from solutions of precursor ingredients. The processes covered here include basic lab scale batch processes, as well as continuous processes which are being used in the research of upscaling perovskite production. Additionally, the latter part of this section gives an overview of solar cells and the methods and figures of merit used to test perovskite films incorporated into solar cell devices.

2.1 PEROVSKITE

Perovskites take their name from a naturally occurring mineral, $CaTiO_3$, which was named for Russian mineralogist Lev Perovski. Crystals that share this structure are also referred to as perovskites including the metal halide hybrid compositions that make up a subset of emerging semiconductor technologies. The structure of these semiconductors is made up of two positively charged ions, A and B, typically of different sizes, which are both bonded to an anion X in the formation shown below in Figure 1.

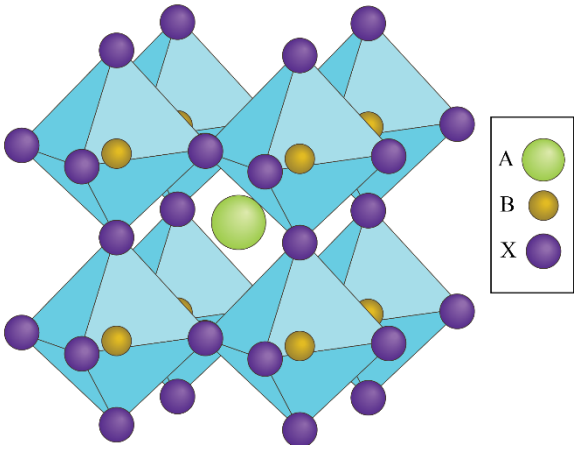

Figure 1 Cubic perovskite crystal structure

A is often an organic cation such as methylammonium (MA), or formamidinium (FA), although a non-organic cation like Cs can fill this role as well. B is a metal cation, often Pb, although lead free perovskites are an expanding topic of research, exploring Sn, Bi, Sb and more as alternatives to lead. X is the halogen anion, typically Cl, Br, or I. Perovskites can be formed from simple combinations such as $MAPbI_3$ as well as more complex ratios such as $Cs_{0.05}FA_{0.85}MA_{0.10}Pb(I_{0.97}Br_{0.03})_3$ with different formulations resulting in perovskites with different properties such as band gap or stability.

One of the most well reported compositions is methylammonium lead triiodide ($CH_3NH_3PbI_3$), which is the focus of this work. Despite the general formula being the same, not every resulting perovskite crystal will have the same properties or electrical behaviour as the crystal morphology, size, alignment, and direction all have a large impact on the electrical performance of the semiconductor. Many perovskites being researched today are made as polycrystalline thin films. Generally, a single crystal film would have superior electrical performance, but this is balanced against the ease of production of polycrystalline films. Polycrystalline films are inferior due to the grain boundaries within the film; it is far easier for charge carriers to move within a single crystal than a poly crystalline film. The two main reasons for this are that a charge carrier must have a sufficient amount of energy to cross a grain boundary, thus confining some of the lower energy carriers[23]; furthermore, it has been observed that grain boundaries have the highest density of trap states, which promote recombination of electrons and holes, reducing the charge carrier density and consequently hindering electrical performance. For these reasons it is desirable for a perovskite film to have larger crystals and a smooth surface to decrease the overall surface area of crystal domains and promote enhanced carrier lifetime.

2.1.1 $CH_3NH_3PbI_3$ Methylammonium Lead Iodide

As previously discussed, perovskite can refer to many different chemical compositions but for the remainder of this text the perovskite that we will focus upon is methylammonium lead iodide ($CH_3NH_3PbI_3$ or $MAPbI_3$). The crystal structure of this compound is cubic at high temperatures, transitions to a tetragonal system at 330K, and an orthorhombic system

at 161K[24]. The calculated X-ray diffraction patterns of the three phases can be seen in Figure 2. This means that the analysis done at room temperature on samples examines the tetragonal phase of the material, although the cubic phase should exist during solution processing. The tetragonal phase of $CH_3NH_3PbI_3$ is generally treated as a direct bandgap semiconductor with a bandgap of 1.59 eV. Although there is some debate on the precision of this figure it serves as a suitable assumption for this work. This system serves as the best candidate for high temperature shearing experiments for several reasons: the material captures a segment of solar radiation underserved by many current silicon solar devices, it is the most commonly reported formulation for perovskite work at large, and the focus of this work also includes employing a unique deposition method (shearing with high temperature solvent engineering). Although there has been promising research into lead free and multi halide perovskite compositions, these materials introduce a great number of variables, and the lessons learned in this work could help build toward experiments with different varieties of perovskite.

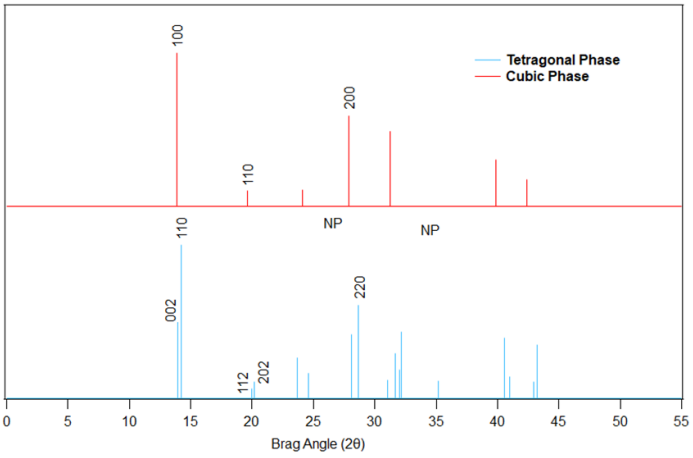

Figure 2 Theoretical x-ray diffraction pattern of MAPbI3 perovskite tetragonal and cubic phases

2.2 SOLUTION PROCESSING AND SCALABLE DEPOSITION METHODS

The solvents used to make the perovskite precursor solution and the deposition method used have a large impact on the resultant perovskite film's morphology.

Perovskite crystals can be created through solution processing. The precursor ingredients of MAI and PBI_2 are dissolved into a solvent to make a precursor solution. A perovskite intermediate taking the form of a Lewis acid-base adduct is formed in the precursor solution, with the metal halide serving as the Lewis acid and the polar solvent as the Lewis base [25]. With the application of heat, the solvent is driven off and the perovskite crystal is constructed with the organic compound. As the solvent is gradually driven off the intermediate compound provides the building blocks to grow the perovskite crystals.

Common solvents for the creation of perovskite precursors are polar solvents with high boiling points such as DMF, DMSO, GBL, and NMP [17,26–29]. The structure of these solvents can be seen in Figure 3. The choice and combination of precursor solvents is a portion of the research field commonly referred to as solvent engineering, with other components being anti-solvent treatment, and solution additives.

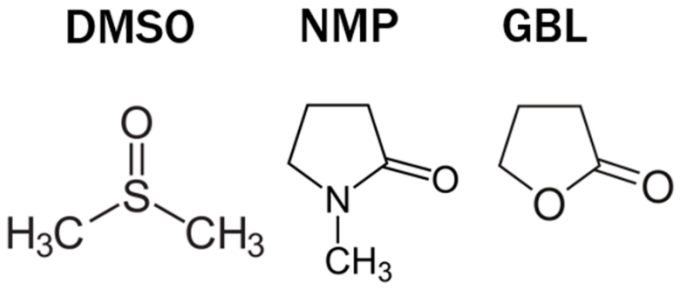

Figure 3 Chemical composition of DMSO, NMP and GBL

Solution processing of perovskite films is done by either a one-step or a two-step method. In the two-step method a solution of the metal halide component (PbI_2) is deposited on the substrate, and then a second solution containing the organic component is deposited on the metal halide layer. After both layers are deposited a heat treatment is performed allowing the organic and metal halide components to react and form perovskite crystals. This process utilizes different solvents for the two steps. The solvent in the second step must dissolve the organic component but not the metal halide component as to not disturb the first layer during the deposition process of the second layer.

The one-step process uses a solvent that can dissolve both components and deposits them together forming a perovskite film in one step as the solvent is driven off in heat treatment [30].

The two-step method showed improvements over the one-step method in spin coated samples but research continues to explore the one-step method, especially in processes more scalable than spin coating [31]. Below is a diagram (Figure 4) of both one- and two-step methods being used with spin coating deposition.

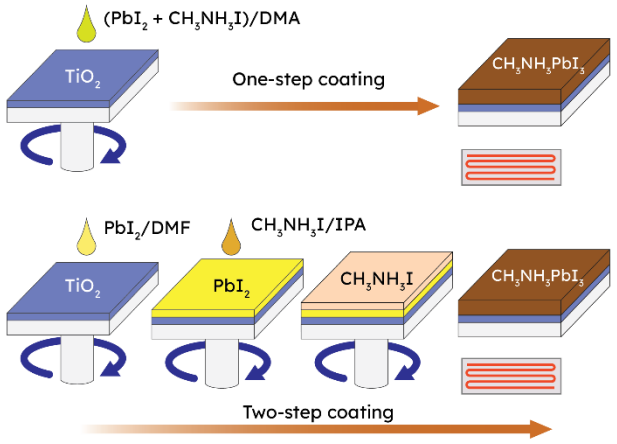

Figure 4 Diagram of one-step and two-step spin coating of perovskite films

2.2.1 Spin Coating

Spin coating is a very common deposition method in perovskite research. In this method the substrate is held on a chuck that can be rotated at a programmable speed, with adjustable acceleration and deceleration. Solution is pipetted onto the substrate and centripetal force moves excess solution off the edge of the substrate leaving a thin, even coating. This method requires relatively simple equipment, and is fast and reliable, making it a popular choice for lab scale experiments. A major downside of this method is that it scales up poorly, generally only serving to make samples up to a couple of inches in diameter.

Spin coating can be done at room temperature, with crystallization happening when the sample is transferred to a hot plate to drive off the solvent. Nucleation happens at random points through the film resulting in a consistent film of many small anisotropic crystals. Studies have found an antisolvent treatment of CB or IPA can be done by dip coating or as a second spin coating operation to promote faster crystallization, leading to smoother films with improved electrical performance[31,32]. Longer annealing processes are sometimes used to grow crystals through Oswald ripening [32].

Deposition methods which have greater potential for scaling up have the capacity for larger batch processing or continuous processing. As opposed to a pipet tip depositing the solution at the center of the substrate, scalable methods start at one end of the substrate and proceed to the other end. This is accomplished by either moving a deposition head or moving the substrate.

2.2.2 Spray Coating

One example of a scalable deposition method is spray coating. In this method perovskite precursor solution is fed to a nozzle where it is atomized and either falls straight down to the substrate below or is carried by pressurized gas. Atomization is mechanically driven by high pressure gas flow, ultrasonic vibrations at the nozzle tip or cavitation of the solution. By either moving the substrate or nozzle relative to each other the nozzle can coat an entire substrate with a thin even layer of perovskite solution [33]. An ultrasonic spray coating diagram can be seen below in Figure 5. Spray coating can be utilized with either the one-step or two-step process, resulting in similar morphologies to spin coated samples [31].

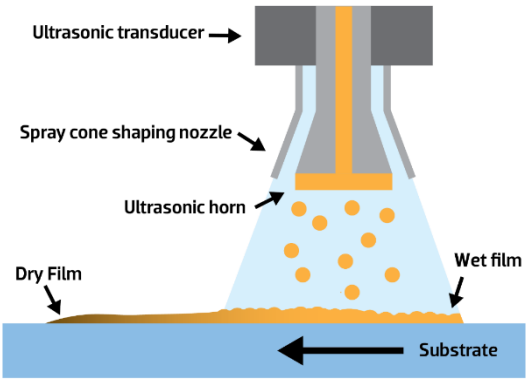

Figure 5 Diagram of ultrasonic spray coating

2.2.3 Ink Jet Printing

Ink jet printing is similar to spray coating but utilizes a different head to opt for a controlled jet of solution, as opposed to a wider atomized spray. The jet of solution is created by increasing the pressure in a microfluidic cavity in the print head, forcing the solution to exit a small hole. The pressure variation can be caused by temperature alteration or mechanical force on the nozzle. Advanced printers commonly use piezoelectric heads that compress the fluid cavity in response to an electrical signal as seen in the diagram below (Figure 6) [2].

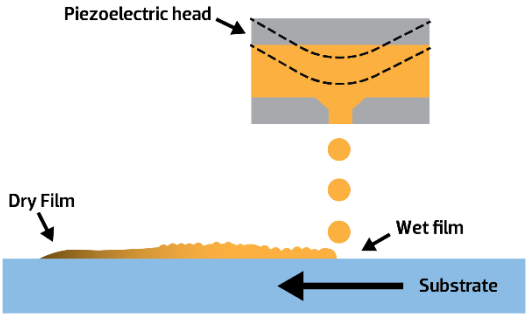

Figure 6 Diagram of ink jet printing

The morphology of films created through ink jet printing are similar to spin and spray coating as these techniques form similar thin films that then crystalize in the same way [34]. Some sources have found that these techniques are preferable for the two-step method. In the one-step process where crystallization happens soon after deposition there is the possibility of overlap in droplets which could suddenly change the chemical concentration in an area or dissolve and recrystallize parts of the film.

2.2.4 Die-Slot coating

Unlike the previously discussed method which deposited droplets of solution onto a substrate, die-slot coating is a meniscus coating method. See below in Figure 7 a die with a thin channel or slot is positioned near the surface of the substrate; the cavity in the die has a controlled feed of percussor solution, and the solution that exits the tip beads up and is held between the die and substrate by surface tension. As the die moves in relation to the substrate the meniscus creates a thin layer of perovskite solution. This method has been shown to produce morphology similar to spin coating, but in other tests has been able to impart a preferred orientation to the crystals of the resultant perovskite film [13].

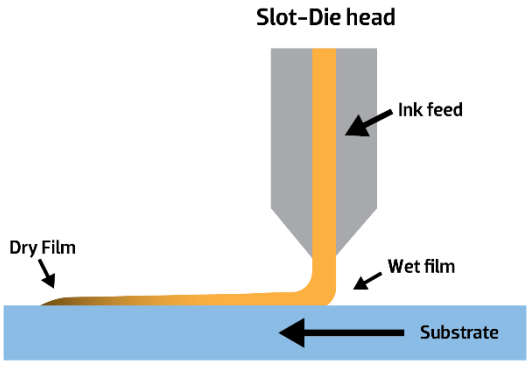

Figure 7 Diagram of die-slot coating

2.2.5 Blade coating

Blade coating is another meniscus coating method that operates similarly to die slot coating, but instead of a finely machined die a thin sharp blade is held near the substrate and perovskite solution is deposited behind the blade. As the blade is moved it leaves a thin layer of perovskite solution, fed from a reservoir which diminishes as the coating progresses. A diagram of this process can be seen inf Figure 8. This method has been primarily used with the one-step process which has been shown like other methods to create films with morphology similar to spin coating, but under different conditions it has shown preferred crystal orientation and parallel crystallization fronts which result in longer crystals [35].

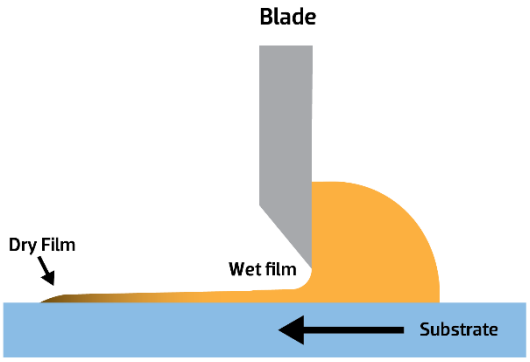

Figure 8 Diagram of blade coating method

2.2.6 Solution Shearing

In this work, we focus on a unique solution shearing method developed in the Koleilat lab. [34,35]. Solution shearing, derived from blade coating, is a scalable deposition technique where the solution is confined between a heated substrate and an angled blade. A diagram of the process can be seen in Figure 9. A key difference between a basic blade coating technique and solution shearing is that high temperatures of the heated substance allow for deposition in the "evaporation regime" where crystallization is happening as the solution

forms a thin layer. This is different from blade coating, which takes place in the Landau-Levich regime, where the layer is deposited and then it crystalizes [3]. This makes blade coating more like spin coating, where the primary impact of the deposition method will be the thickness of the fluid layer. The angled blade and temperature management of solution shearing enables control over the solution meniscus, helping control solvent evaporation and the crystallization process. Film thickness and crystal morphology are tuned by varying the nature and concentration of the precursor solution, the type of solvent used, its polarity and boiling point,[1]what chemical additives are used (e.g., MACl), the temperature of the heated platform, the blade speed, the gap between the blade and substrate, the volume of solution used, and the dimensions and angle of the blade.[37,38]The heated base adds complexity to the process but allows the creation of films with large highly oriented crystals from various solvents, without the use of chemical additives (that could increase grain size further but affect the cost, complexity, bandgap and exciton binding energy of the material),[39] solvent quenching, or the application of a vacuum environment.[40] Solution shearing was chosen as the primary deposition method for this work because of its compatibility with large scale deposition and the ability to carefully control the various deposition conditions, leading to a carefully engineered film morphology[1]. Not all of the above-mentioned parameters were varied and the chosen parameters are discussed in detail within Chapter 3.

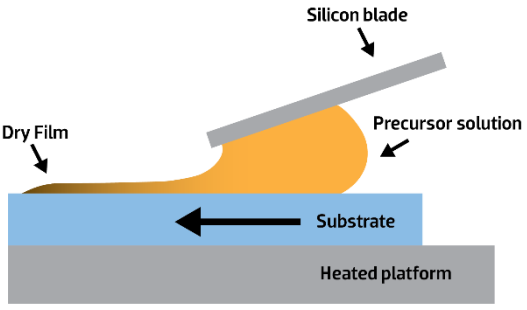

Figure 9 Solution shearing process.

2.3 SOLAR CELL INTEGRATION

Perovskite can be incorporated into different types of semiconductor devices, with solar cells being one application that garners a lot of attention due to its tunable band gap and potential for lost cost manufacturing. Previous work from the Koleilat group had success with photodetector devices but this work was well timed to expand into preliminary solar cell implementation testing.

Perovskite solar cells differ in some ways from traditional solar cells see below in Figure 10. This section will provide information on the basic construction of a traditional solar cell and highlight the differences in a perovskite solar cell (PSC).

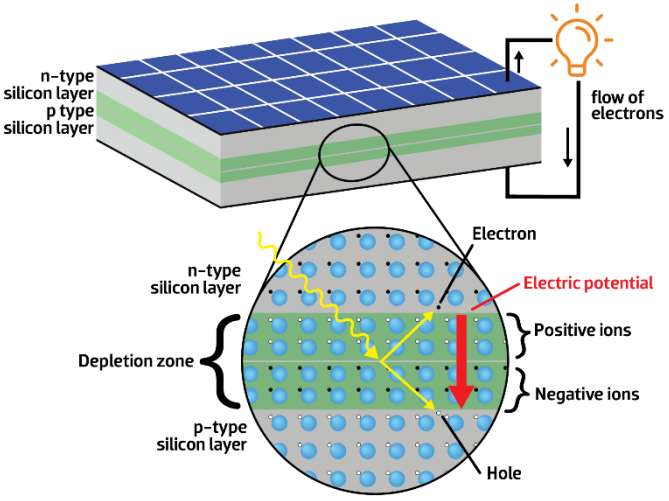

Figure 10 Silicon solar cell

Solar cells have a semiconducting layer at their center. In a traditional cell, this layer is made from a single silicon crystal. This crystal utilizes certain amounts of impurities to alter the number of electrons present in the material in a process called doping [41]. In one half of the crystal, the most abundant secondary element after Silicon would be Phosphorus. P has a greater number of electrons than Si, so this portion of the crystal is more negatively charged and is referred to as the n-type silicon layer. In the other half of the crystal, the most abundant secondary element after Silicon is Boron. Since B has one fewer electron than Si, it has a more positive charge making it the p-type silicon layer. This lower number of electrons can also be thought of as an increased number of "holes" where electrons would

be. Holes can be thought of as their own particle, the positive counterpart of an electron. Both electrons and holes are called charge carriers and the movement of these charge carriers in a material is the flow of electricity. These two regions of the silicon crystal meet at the PN junction. The area at the PN junction becomes depleted of charge carriers where the excess electrons at the edge of the n-type region fill the holes at the edge of the p-type region. This leaves positive ions on one side and negative ions on the other, which creates an electrical potential difference across the region.

In contrast, Perovskite solar cells differentiate themselves in terms of structure as the semiconductor layer does not require further doping. While the traditional solar cell typically uses a PN junction, perovskite cells typically use a PIN or NIP junction. An example of both structures can be seen in Figure 11. The choice between junctions dictates the materials used for the transport layers. This project chose to work with an NIP structure allowing for the use of ITO (indium tin oxide) and SnO_2 as transparent conductive materials. To make up this junction, the perovskite layer is sandwiched between a hole transport layer (HTL) and an electron transport layer (ETL). The electron transport layer is made from a material with an abundance of electrons and allows for easier movement of electrons from the perovskite into the device's contacts. The same phenomenon is applicable for HTL and the movement of holes. The presence of these two layers creates a potential difference across the solar cell which informs the flow of carriers generated in the perovskite layer [42].

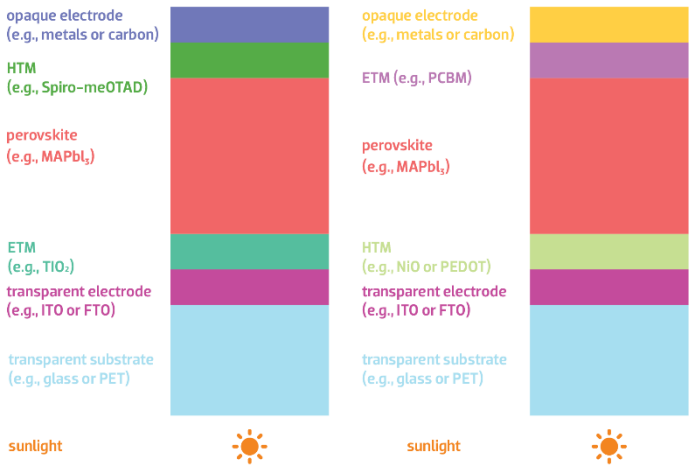

Figure 11 NIP and PIN architectures of perovskite solar cells

Within a solar cell, the role of the junctions is to create an electric field in which the electrons and holes generated are separated by photons emitted from the sun. When a photon passes through the upper layers of the solar cell and strikes an atom in the silicon crystal, it imparts energy which frees the electron from the atom to create an electron-hole pair. This pair recombine with each other to create light and heat within the crystal, but the potential difference across the depletion zone provides pressure for the carriers to go off in opposite directions and contribute to the flow of electricity. One carrier flows to the metallic back contact of the solar cell, while the other flows to the front. The front contact layer of a solar cell cannot fully cover the surface with a metallic contact as we need to maximize transparency to allow light into the semiconductive layer. Front contacts often utilize a layer of transparent conductive material such as ITO with thin metallic busbars. These contacts lead to a junction box built into the frame of the solar panel where it can interface with a larger electrical system. Other layers of the solar cell include anti-reflective coatings and aluminum casing.

2.3.1 Recombination

Perovskite solar cells (PSC) and other perovskite devices often use polycrystalline semiconductor components due to the increased difficulty of creating single crystal perovskites. The morphology of the polycrystalline films affects how the electrons and holes in the material behave, particularly when they recombine. There are three main modes of recombination in perovskites: trap-assisted, bimolecular, and Auger, as shown in Figure 12 Diagram showing recombination mechanisms in halide perovskite. Bimolecular is a radiative process where an electron from the conduction band (CB) and hole from the valance band (VB) combine to produce a photon. Trap-assisted recombination is a monomolecular, non-radiative process where a carrier moves to a defect induced localized energy level between the VB and CB. Auger recombination is a non-radiative process where a carrier transmits its energy to a carrier of the same type allowing it to recombine.

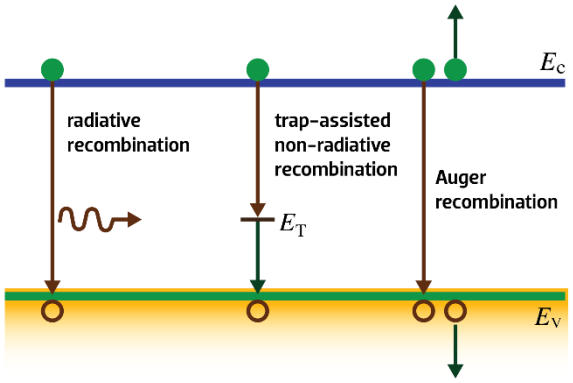

Figure 12 Diagram showing recombination mechanisms in halide perovskite

Bimolecular Recombination

Bimolecular recombination is present in any direct bandgap semiconductor and is preferred to the other forms of recombination because it is radiative. This is favourable as it contributes to an increase in photon density within the material, resulting in a higher

operating voltage for perovskite devices [41, 42]. The other two types of recombination are non-radiative and are generally considered loss mechanisms.

Trap-Assisted Recombination

Trap-assisted recombination is a form of non-radiative recombination facilitated by a trap site such as an impurity or a crystal defect [44]. Trap state density has been found to be higher at the surface of perovskite crystals than in the bulk [44–46]. Trap states can lead to losses, but not all trap states are created equal. Shallow trap states are preferentially formed in lead halide perovskites [47]. These trap states exist near the conduction or valence band and are less detrimental to performance than deeper trap states. Carriers trapped in shallow states can be easily freed by a small amount of energy, while deep trap states facilitate easier recombination and thus greater losses [42,48,49].

Auger Recombination

The other form of non-radiative recombination is the Auger recombination, which becomes the dominant mode of recombination at very high carrier concentrations, making this type of recombination much more common in perovskite LEDs than other devices like solar cells [45,50].

From this look at recombination methods it is clear that a way to improve perovskite performance is to reduce the number of trap sites, which can be accomplished by minimizing grain boundary area. This makes large crystal size an indicator of quality in perovskite films. Logically this work aimed to expand upon the Koleilat Group's projects that had produced the largest crystals.

2.4 STRATEGY

Perovskite material has faced many challenges throughout the last decade in a push to close the gap with other semiconductor-based research for optoelectronic applications. The

Koleilat research group previously focused on producing large scale stable perovskite thin films to be used in photodetector applications. The group reported highly oriented macroscopic crystal grains made from MAPbI3 in DMSO, a polar solvent with a boiling point of 189°C [35,51]. Other studies have reported blade coated $MAPbI_3$ in another polar solvent, N,N-Dimethylformamide (DMF), at various temperatures, which has led to much smaller crystalline domains [37,52]. Although DMF has a similar boiling point (153°C) to DMSO, it has been mostly kept to low temperature film fabrication with spin coating due to its viable use within the parameters of a technique where DMSO based solutions have struggled. Considering the encouraging results previously obtained and the scalability issue mentioned earlier associated with spin coating, further exploration of MAPbI3 deposition at high temperatures was decided on. The was aim to produce perovskite thin films that maintain the stability goals previously achieved, while taking full advantage of the increased temperature by testing greener solvents such as GBL or a mixture of solvents, as they proved to yield a better photoresponse from perovskite semiconductors.

Ideally, a single crystal thin film would be used for multiple optoelectronic applications. In practice, film morphology is highly dependent on the solvent evaporation rate during the solution shearing method. Therefore, the work for this project investigated the effects of employing higher boiling point solvent mixtures with DMSO, potentially slowing the evaporation rate, and affecting the crystal formation of $MAPbI_3$. GBL and NMP have higher boiling points (204°C and 202°C respectively) and coordinate with the perovskite precursor ingredients to form Lewis acid-base adducts [26,39,53]. Of all the solvents used to dissolve perovskite precursors, DMSO has the strongest coordination, followed by NMP and then GBL. These two solvents have attracted attention as greener alternatives to DMF, and as additives in precursor mixtures [54–56]. Much of the research into these solvents has been performed at ambient temperatures, therefore it was expected to see different results when exposing these combinations to over 150°C temperature in the solution shearing technique. Due to its high viscosity and slow evaporation rate, DMSO has resulted in poor MAPbI3 crystal formation when employing temperatures lower than 150°C but was shown to produce high quality crystalline thin films when used as the main precursor solvent for solution sheared MAPbI3 deposited at higher temperatures [57].

Evaluating the suitability of solvent mixtures will enable reliable fabrication of uniform highly organized crystalline films. This evaluation prioritized large uniform crystals which are likely to have fewer surface defects and grant superior electrical properties, among which is a reduced recombination rate. The work relied on SEM and optical microscopy to characterize the morphology, powder X-ray diffraction (XRD) and grazing incidence wide angle X-ray scattering (GIWAXS) to observe preferred crystal orientation and identify non-perovskite crystal phases and twin domains[58], and photoluminescence spectral responses to identify the presence of unfavorable recombination modes. These studies revealed that a mixture of lower and higher boiling solvents, here DMSO and NMP, lead to much higher quality films with larger crystal grains and uniform coverage.

2.5 LITERATURE REVIEW

Recent literature has tackled various issues faced in perovskite-based optoelectronic devices. I will discuss the relevant research that inspired and educated our approach to the proposed thesis. In 2017, Huang et al utilized spit coating of $MAPbI_3$ perovskite at room temperature with binary and trinary solvent mixtures of DMSO, GBL and DMF. They found that DMF solutions had poor coverage and did not produce viable solar cells. The researchers expressed their results in terms of PCE and found that GBL solutions produce the lowest efficiencies at 1.74%, much lower than DMSO based cells at 8.37%. The 1:1 mixtures DMSO:DMF and DMSO:GBL were 7.64% and 9.77%. Their best mixture was a trinary mixture of DMSO: DMF:GBL (5:2:3) with a PCE of 10.84%. [17] This showed the promise of GBL as an additive even if initial GBL results were poor. On the other hand, Arain et al. experimented with adding DMSO to NMP precursor solutions for room temperature spin coating and low temperature annealing. They found that adding up to 30% DMSO produced pin-hole free films and improved solar cell PCE from 16% to 18%. This showed the benefits of both the DMSO and NMP intermediate compounds at both low temperature deposition and annealing.[59] As for Chen et al., they compared MAPbI3 perovskites with mesoporous substrates deposited with DMSO, NMP, GBL, and DMSO:DMF mix solutions. They analyzed all their films using PL and ran PCE testing on

their champion device, which produced from the DMSO:DMF mixed solvent a 13.48% PCE. They also tracked and compared the presence of intermediate compounds before and after annealing using XRD.[60] Kim et al. studied the morphology of sheared $MAPbI_3$ solutions in a DMSO:DMF mix. By varying speeds up to 5mm/s and temperatures up to 150°C, they identified different regimes with distinctly different morphologies. They found that higher temperature shearing produced much larger crystal domains and emanated micro-wire structures.[37] Li et al. for instance utilized solution shearing of $MAPbI_3$ with DMF precursor solutions to make highly oriented crystals on flexible substrates. They used a speed of 0.2mm/s at a temperature of 100°C to create a perovskite film and compared its stability to a film of randomly oriented smaller crystals. After 48 hours in a 50-60% relative humidity environment, the current output of the sheared device degraded by 17% and the control device by 90%.[38] Deng et al. performed high speed, room temperature blade coating utilizing nitrogen gas flow to speed evaporation. Precursor solvents included DMSO, GBL, DMF, 2-methoxyethanol and acetonitrile. Their champion device was created blade coating at 99mm/s with a solvent mix DMSO, 2-methoxyethanol and acetonitrile. This device had a PCE of 16.4%.[61] Li et al compared blade coated perovskite films made using DMSO and GBL mixed solvents at 25°C and 150°C. They found larger crystals were produced from the high temperature blade coating, theorizing that the evaporation and deposition rates align to leave the solution at ideal saturation during the deposition process. They achieved a PCE of 17.85% from their best mix solvent sheared device.[57] Hasan et al. experimented with shearing of DMSO perovskite solutions at temperatures of 150°C-170°C. They found that temperatures of 160°C and 170°C produced larger crystalline films. When incorporated into a photodetector, the sheared sample had improved responsivity and external quantum efficiency when compared to spin coated baseline. The sheared devices maintained 80% of their efficiency over two weeks.[35] Nie et al. spin coated perovskites on substrates heated between 130°C and 202°C, using DMF and NMP as high temperature solvents. They found that the use of high boiling point solvents increased crystal growth and produced a perovskite solar cell with a PCE of 18% [46]. As well, Yang et al. created blade coated perovskites at room temperature from DMF, DMF:NMP, and DMF:DMSO solutions. They achieved the highest efficiency using a NMP:DMF solvent mix and created large area solar cell with 17.33% PCE.[62]

2.6 CONCLUSION

High temperature shear coating remained an unexplored area of solvent engineering in perovskite materials. The literature showed that there were benefits to producing films at a temperature near the solvent's boiling point and utilizing a scalable method. Shearing was selected for its low opportunity cost and tunable parameters. compatibility with high temperatures. To the best of our knowledge the possible morphologies of this combination solvent engineering and deposition method were unreported in literature. Results of this work would also be combatable with other areas of research such as surface passivation and film post processing, suggesting promising results could be applied to future research.

CHAPTER 3 METHODS

Chapter 3 overviews the techniques, tools, and materials used in preparing and evaluating the MAPbI3 perovskite thin films and devices. Some preliminary results are displayed to aid the discussion.

3.1 SOLUTION PREPARATION

The first step in creating a perovskite thin film is to mix the precursor solutions. The solutes used were lead iodide (PbI_2, 99%), methylammonium iodide (MAI ≥99% anhydrous), and the solvents used were dimethyl sulfoxide (DMSO anhydrous, ≥99.9%), γ-butyrolactone (GBL anhydrous, ≥99%), 1-methyl-2-pyrrolidinone (NMP anhydrous, 99.5%). All ingredients were purchased from Sigma-Aldrich.
The $MAPbI_3$ precursor solution was produced by dissolving a 0.3M equimolar ratio of PbI_2 and MAI into a solvent or two-solvent mixture with a 1:1 volumetric ratio. Solutions were stirred at 400 rpm at 70°C for 7 hours prior to shearing. Preliminary work was done with other volumetric ratios including 3:1 and 4:1, but this was not done for all combinations.

Early in this project DMF (N,N-dimethylmethanamide) was going to be tested along with DMSO, GBL and NMP. These solvents were common in perovskite literature and thin films made from solvent combinations such as DMSO and DMF had promising electrical properties[60]. DMF was cut from the scope of this project because perovskite films made from DMF precursor proved to be inconsistent, highly unstable, and difficult to characterise. It was believed that the reason for these poor results was the high temperature of the chosen perovskite deposition method. In cases where films could be sheared with good substrate coverage, fast evaporation of the precursor solution would often result in burnt, wire-like films, or films where all the solvent was not driven off, resulting in

recrystallization within the grains. Failed films produced with DMF can be seen below in Figure 13.

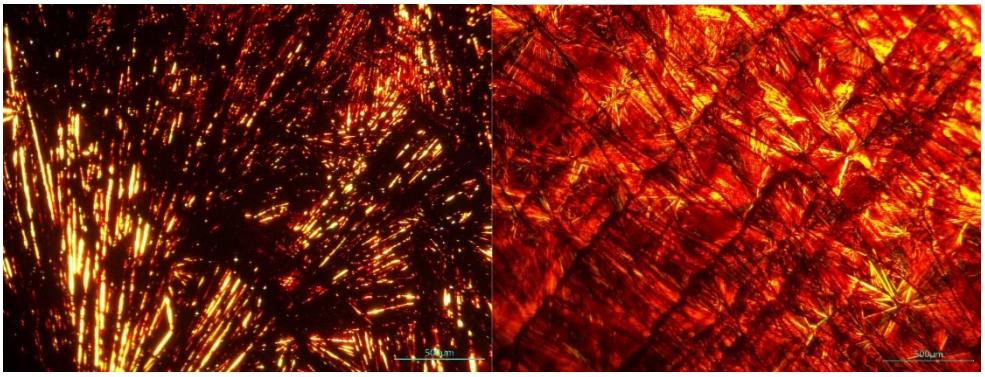

Figure 13 0.3M Perovskite solutions in DMF sheared at 170°C (left) and 158°C (right)

Before being cut entirely, work with DMF solutions progressed to altering the molarity of the film to compensate for the fast evaporation rates when sheared. Range finding experiments were performed from 0.3M to 0.1M under various temperatures searching for films that had well defined large crystals without signs of burning or degradation. Solutions of 0.13M were found to have the fewest issues.

3.2 SHEARING

The primary perovskite deposition method used in this project was solution shearing. Solution shearing, derived from blade coating, is a scalable deposition technique where the solution is confined between a heated substrate and an angled blade. The shearing station used in the project was custom built for the Koleilat Lab, as shown in Figure 14.

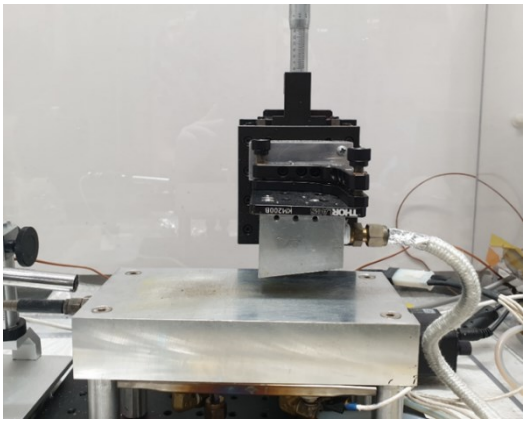

Figure 14 Shearing station

Shearing was performed with 60 µL of solution at elevated temperature (140-170°C) on a 25 x 25 mm glass substrate. The gap between the blade and substrate was 300 µm and the blade moved at a set speed (0.100-0.125 mm/s). Temperature and shearing speed were refined for each solvent as listed: DMSO: 150°C, 0.100 mm/s; GBL: 170°C, 0.125 mm/s; NMP: 170°C, 0.125 mm/s; s-DG: 170°C, 0.115 mm/s; s-DN: 170°C, 0.115 mm/s; s-GN: 170°C, 0.125 mm/s. Sheared films stayed on the heated platform for 4 minutes before being moved to a hot plate where they were annealed at 100°C for 20 minutes under an inert nitrogen atmosphere.

The choice of this technique contributed to making the research novel. Solution shearing enables control over the perovskite precursor solution meniscus, helping control solvent evaporation and the crystallization process by modifying the station's temperature and the speed of the blade. The combination of this technique with solvents of different polarity, viscosity, and boiling points allowed for the creation of perovskite films with varying thickness and crystal morphology.

3.2.1 Shearing speed

To determine shearing speed for each solvent there were two experiments. The first incrementally increased the speed by 0.01mm/s with the goal of determining the best substrate coverage. Poor substrate coverage was primarily a result of an unclean substrate, but speeds that were either too high or too low could result in gaps in coverage. A second

experiment was performed after an optimized temperature was found for each solvent: this experiment incrementally raised the shearing speed by 0.005mm/s for two increments above and below the current speed with the goal of optimizing for larger crystal size.

3.2.2 Shearing temperature

Finding the temperature to shear each solution was done by performing a range finding experiment of shearing the same solution multiple times and altering only the temperature by increments of 10 °C. At this stage of the project, the goal was to create films of large crystals, so the primary screening metric to determine which temperature was best was crystal size. However, other considerations were made for temperatures that produced visible flaws or signs of degradation of the perovskite crystals. With a focus on higher temperature, shearing temperatures ranged from 150 °C and up. Experiments at 190 °C and 200 °C provided an upper bound based on initial results. There were two noticeable issues shearing at these higher temperatures (above 190 °C); although large crystals could be made at these temperatures the surfaces were very inconsistent. The fast evaporation left a surface that appeared marred and damaged, and the shearing setup heated the substrate evenly, so the end of the film that was deposited first was exposed to the heat longer than other portions of the film. It was at grater than 190 °C that this extra time became notable, with portions of the film burning and reacting with the air resulting in degradation. An example of film displaying these notable production issues can be seen the figure below.

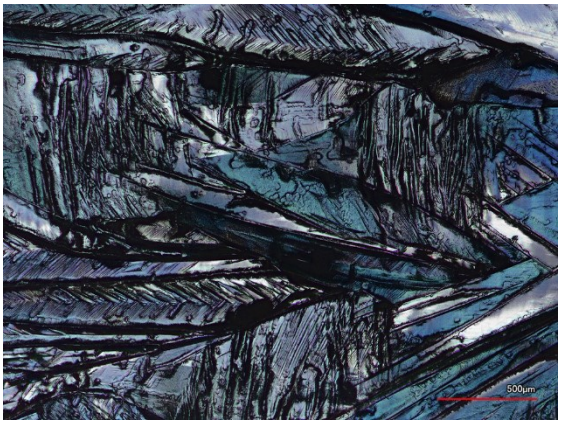

Figure 15 s-DMSO solution sheared at 190°C. Films sheared at high temperatures contain large crystals but are marred by ripples and gouges. Films sheared at high temperatures can possess blue surface coloration as well as blackened spots

3.2.3 Shearing solution volume, and shearing blade gap

The initial values for these variables were based on previous work of the lab group and were not optimized in this project. There were some small experiments with these values when trouble shooting but they ended up staying constant.

Table 1 Average roughness and thickness of all samples measured using laser confocal microscopy.

Sample[)]	Sa [um]	Thickness [um]
s-DMSO	0.67	0.714
s-GBL	0.57	1.305
s-NMP	0.57	1.867
s-DG	0.73	1.586
s-DN	0.57	1.533
s-GN	0.57	0.959

3.3 MICROSCOPY

The morphology of perovskite films was assessed using a Keyence laser confocal microscope (VK X-1000) and a Hitachi S-4700, cold field emission SEM (scanning electron microscope). The confocal microscope was used at magnifications from 50x to 500x to quantitatively measure the surface roughness and thickness of the film, as well as to qualitatively assess the films. The SEM was used to support the evidence of the confocal microscope with high magnification pictures and to photograph a perovskite device cross section. SEM photographs of perovskite films can be seen in Figure 16 and Figure 17.

The morphology of the polycrystalline perovskite films was directly related to the film's electrical properties. Small grain size and high surface roughness were indicative of undesirable electrical properties. Also signs of degradation, burning, or contamination not obvious to the naked eye could be seen with an optical microscope. This allowed for early range finding experiments to determine the shearing parameters for each solvent to be done quickly, before using multiple characterization techniques to optimize them.

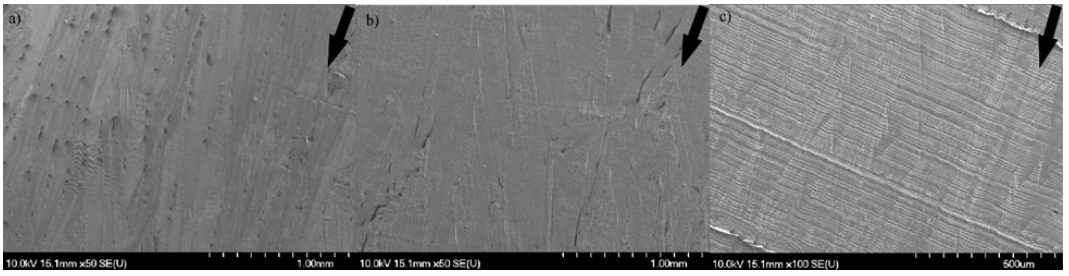

Figure 16 SEM images of high temperature solution sheared perovskite films produced from a) DMSO, b) NMP, and c) GBL solutions.

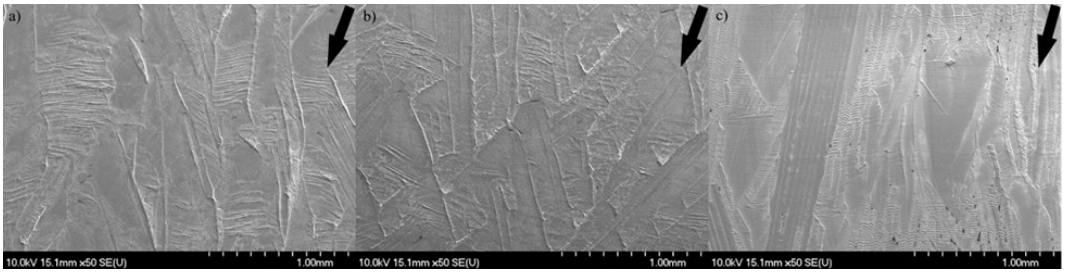

Figure 17 SEM images of high temperature solution sheared perovskite films produced from mixed solvent solutions with a (1:1) ratio; a) s-DG (DMSO:GBL), b) s-DN (DMSO:NMP), and c) s-GN (GBL:NMP)

SEM was performed on samples of all the solvent combinations but due to the increased time it took compared to confocal it was not the primary means of surface evaluation. At high magnification the SEM could display the surface of an individual grain which was generally unremarkable. At lower magnification it was able to provide similar information as the confocal.

3.4 X-RAY DIFFRACTION

XRD can produce unique diffraction patterns for crystalline phases like those seen in Figure 2 . To create these patterns a sample is placed between an X-ray source and detector. The sample is bombarded with X-rays of a known wavelength while the angle between the detector and source is changed over time. Peaks in the diffraction pattern are created at angles where the incident X-rays diffract off the ordered atoms in a crystal plane and create constructive interference in accordance with Bragg's Law[63]. Where λ is the wavelength of the x-ray, d is the space between planes, θ is the incident angle, and n is an integer

$$n\lambda = 2d\,sin\,\theta$$

Equation 1 Brag's Law

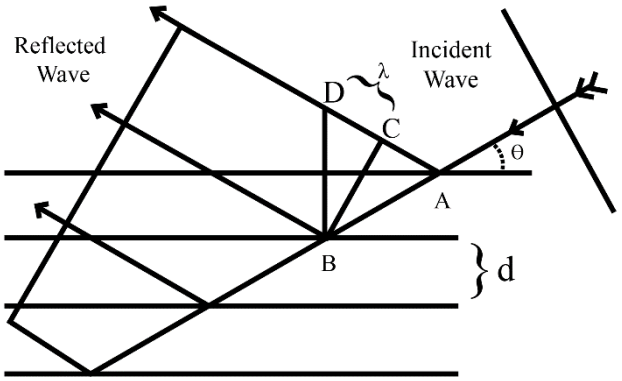

Figure 18 Drawing visualizing Brag's law where incident x-rays at angle θ reflect from crystal planes at both A and B given interplanar spacing d and wavelength (λ) DC

Polycrystalline perovskite films were analyzed by XRD. The analysis of the films was performed with a Bruker D8 Advance X-ray diffractometer using Cu Kα as the radiation source. Perovskite films were scanned while rotating from a 2θ angle of 5° to 50°. This was performed on films that were made within 1 day and had been stored in a controlled atmosphere. The results were qualitatively compared to the expected pattern of the tetragonal $MAPbI_3$ phase.

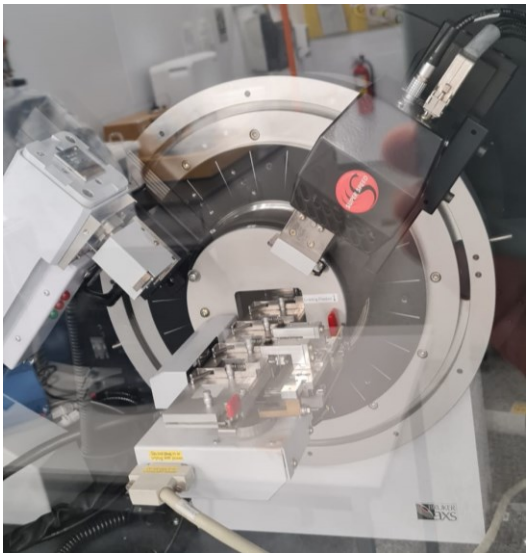

Figure 19 Bruker D8 Advance X-ray diffractometer with X-ray emitter (left), detector (right) and eight sample rotatable stage

This analysis allowed for the identification of non-perovskite phases, such as precursor chemicals, intermediate solvent phases, and products of degradation. This was used to

identify errors in the process as well as unique effects of the process. In addition, on identifying non-perovskite phases, the peaks within the perovskite phase could have the relative peak heights compared. Films that deviated from the expected pattern were suggested to have preferred crystal orientation that had been promoted in deposition.

3.5 GRAZING INCIDENCE WIDE ANGLE X-RAY SCATTERING

GIWAXS is a form of XRD primarily used to characterize nano structures and thin films. The technique uses a 2D area collector to map X-rays scattered from a small area of a sample's surface. The low grazing angle of the X-rays is controlled by tilting the sample by small angles, typically between 0.05° and 0.5°[64] The geometry of a GIWAXS scan can be seen below in Figure 20 [65]. The 2D image resulting from GIWAXS is made up of dots and/or lines which can provide information about the order of poly crystalline films.

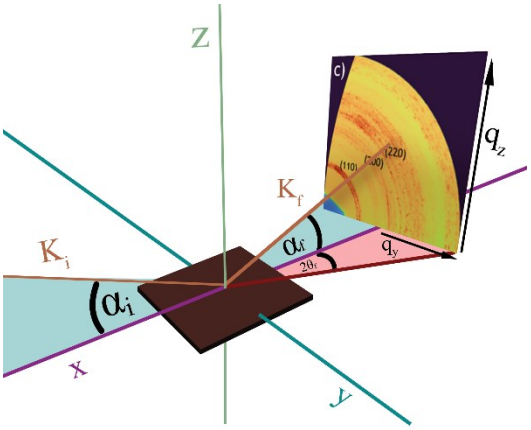

Figure 20 Geometry diagram of GIWAXS of sample and 2D detector

GIWAXS data was acquired at the Canadian Light Source in Saskatchewan using a 15.1 keV energy source. A lanthanum hexaboride sample was used for calibration. GIWAXS data is analysed with GIXSGUI36 and a custom program that automatically computes GIWAXS images.

GIWAXS served as a tool to compare with the gathered XRD data and clarify the structure of the perovskite films.

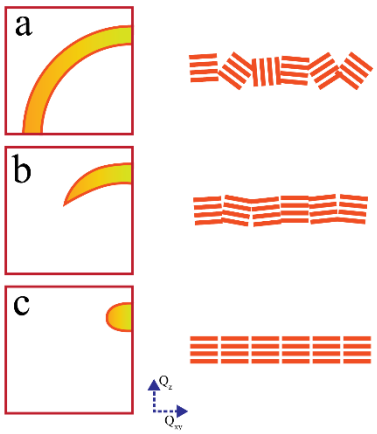

Figure 21 Illustration of the GIWAXS patterns resulting from different orientations of crystals in a poly crystalline film; a)Randomly oriented films produce a full ring, b) Crystals with a preferred orientation produce a short blunt arc, c) highly orientated films produce sharp spots.

3.6 SPIN COATING

A Laurell WS-650 series spin processor was used for depositing perovskite and spiro-MeOTAD. Perovskite was deposited in ambient air, and spiro-MeOTAD in a nitrogen atmosphere glove box. To create perovskite films the substrate was accelerated to 2000 rpm over 10 s, then spun for an additional 10 s. The substrate was then accelerated to 4000rpm over 4 s, and spun for an additional 20 s. During the final 5 s of the spin cycle, the film was rinsed with 200 µL of room temperature chlorobenzene.

Spin coating was performed on perovskite to provide context to compare shearing results against. Due to the popularity of this method, it was important to include at least one film created with the same environment as the shear coated samples to help situate the work of this project within the broader perovskite landscape. This method also served as one of two options, along with shearing, to apply the spiro-MeOTAD Hole conducting layer, although shearing provided the best results.

3.7 THERMAL EVAPORATION

Thermal evaporation is a physical vapour deposition method that uses electric resistance heat in a high vacuum environment to deposit thin layers of metal onto a substrate. A schematic of a thermal evaporation system can be seen below in Figure 22.

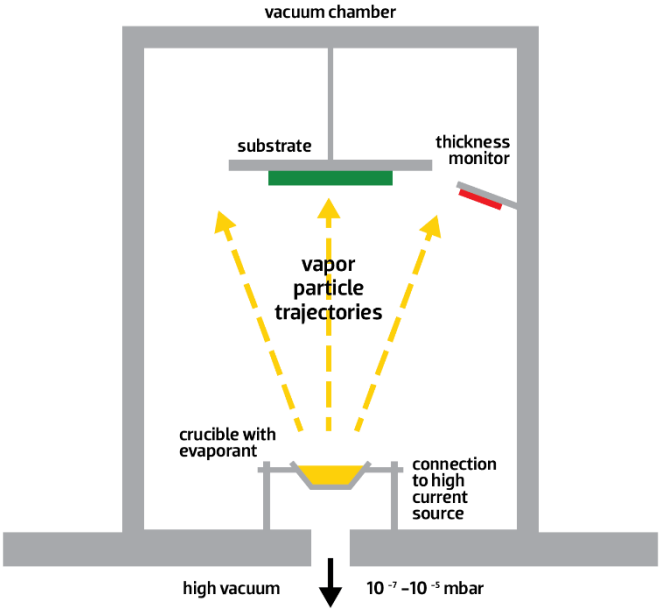

Figure 22 Thermal evaporation chamber

Evaporation was performed in an Mbraun glovebox integrated evaporator controlled by an Inficon SQC310 film deposition controller. The device was mounted upside down to a masked holding plate at the top of the evaporator behind a servo-controlled shield plate. The mask on the holding plate provided the pattern for the gold contacts. Gold was placed in a tungsten boat which served as an electrical resistance heater. The evaporation chamber's pressure was reduced to at least 10^{-5} bar and the power to the tungsten boat was ramped to 28% power supply capacity. When a steady state of gold deposition on the sensor was achieved the shield plate was moved and a 0.15 mm layer of gold was deposited on the HTL surface. The power supply was turned off and the device was left to cool under vacuum overnight. Evaporation allowed for the precise deposition of the metal contracts on top of the HTL which completed the device and allowed for device testing.

3.8 PHOTOLUMINESCENCE

Photoluminescence spectroscopy uses tunable high energy light to excite electrons on a photoreactive sample. A light detector is positioned to collect photons produced from the radiative recombination of those electrons. The intensity and wavelength of light detected can provide information on recombination rates as well as the band gap of the material. The optical systems included in the diagram are often filters or monochromators. The system before the sample ensures that only light of the desired wavelength strikes the sample. A combination of sample position and filtering between the sample and the spectrometer can be used to remove all incident light that may be reflected or scattered. A generic experimental PL set-up can be seen below [66].

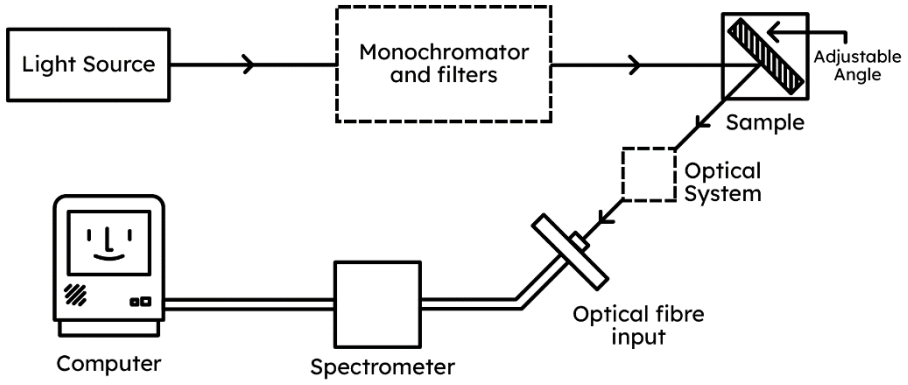

Figure 23 Diagram of a photoluminescence spectroscopy system

The photoluminescent testing was performed with a Horiba Duetta fluorescence and absorbance spectrometer with an excitation wavelength of 670 nm for all tests; a redshift in the data caused by detector inefficiency was corrected.

We measured the photoluminescence (PL) of the various films. PL, where films absorb incident light with higher energy than their main optical transitions, allows us to determine the fundamental radiative characteristics of the films: excited generated electrons should return to the ground state by emitting photons at the optical transition. Trap-assisted non-

radiative recombination quenches the PL intensity, therefore better crystallinity is associated with higher PL intensity [67].

PL of different films served as an indication of their quality and potential performance in optical devices. When the films absorbed light with higher energy than their bandgap, subsequently the created electrons and holes would recombine. Crystals with high volumes of defects and trap states would promote trap-assisted recombination and would not output light matching the energy level of the band gap, therefore not contributing to the intensity of the PL measurement. Electron hole pairs that underwent the radiative recombination would produce light at the expected energy level and contribute to the intensity of the measurement. When comparing films of the same thickness a lower PL intensity could correlate with an increased density of undesired crystal features, making it a worse candidate for optical device integration.

3.9 ABSORBANCE SPECTROSCOPY

Absorbance spectroscopy measures the intensity of light absorbed by a material as a function of wavelength. A film is placed between a tunable light source and a detector which measures the light which passes through the sample at each given wavelength. This can inform which wavelengths a photoactive material is best at harvesting as well as determine the band gap of that material. The Horiba Duetta used for absorbance testing in this work can be seen below [68].

Figure 24 Duetta fluorescence and absorbance spectrometer

Absorbance testing was performed with a Horiba Duetta fluorescence and absorbance spectrometer in the wavelength range of 850nm to 500nm. The data gathered was presented as absorption vs wavelength for qualitative references and as a Tauc plot to identify the band gap of perovskite films.

3.10 DEVICE TESTING

Solar cells were tested by measuring current across two contacts in individual pixels on the cells while performing a voltage sweeping from -5V to 5V. Each cell was tested across 8 different pixels under both dark and light conditions.

The solar cell's parameters were calculated by measuring the current density−voltage (J−V) characteristics under one sun illumination (100 mW/cm^2) at calibrated AM1.5G condition. The current – voltage (I-V) measurements were carried out in a N_2 filled glovebox using a Keithley 2400 source measurement unit. A solar simulator (Sciencetech Model SLB150/300) with Xenon arc lamp was used and the light was calibrated using a solar power meter (SOL-METER, Sciencetech) with the sun calibrated reference detector attachment.

Figure 25 Solar cell testing apparatus with solar simulator mounted below the glovebox and solar cell mounting plate and contacts inside glove box

Power conversion efficiency was tested over time to track the solar cells stability; normalizing the subsequent measurements to the first, this allowed tracking of the cell's degradation. Stability was a prime interest due to the unexpected phases that had been present in some samples and a significant change in performance should indicate problems caused by these potentially unstable phases.

3.11 SAMPLING

The experimentation in the work relied heavily on testing duplicate perovskite films. All experiments in the work were performed multiple times on multiple films or devices. Testing multiple films helps root out outliers and mistakes and allows for the collection of data that is representative of the work.

When precursor solutions were created a duplicate of each solution was made. When solutions were sheared, two testing films were made from each solution. If signs of contamination were observed in one of these test films, it would not be used in that day's experiments. This was a rare occurrence, but having a backup of each solution meant that if one was contaminated all conditions and solution compositions could still be tested on the same day. When films for characterization were created two films were created for each solution chemistry and each set of shearing conditions. Two films were also created for each characterization method. During experiments where there were different solvents and solvent mixtures being compared all films were made on the same day, which created tight time constraints. This is why duplicates were used instead of triplicate. There were some situations such as PL testing and tuning shearing conditions for each solvent mixture where time permitted creating three of each film. As conditions were tuned, multiple batches of samples were tested using both microscopy and XRD; tests that were only permitted to be performed once due to limited available time frame were PL spectroscopy, GIWAXS, and PCE testing.

When analysis data produced from this work all triplicate measurements were averaged and outliers excluded where necessary, with the exception of XRD data where a representative

data set was shown from sample three or more sets. Significance testing was to be primarily focused on the PCE output of the final solar cells created in this work. Baseline samples had their PCE testing in three different labs and it was found that results were constant relative to each lab but different greatly magnitude between the labs. For this reason the PCE measurements were not reported instead reporting the relative PCE over time.

3.12 CONCLUSION

In this chapter, the experimental conditions were detailed with a focus on the different parameters of the shearing technique, the different microscopy approaches used, thin film characterizations employed such as XRD, GIWAXS and PL, as well as additional deposition methods and device testing conducted. Next, the experimental results obtained from the experiments ran in Chapter 3 and the subsequent characterizations will be expanded upon and discussed, focusing on the key outcomes of this research.

CHAPTER 4 EXPERIMENTAL RESULTS

The results obtained are considered in this section, with a discussion and analysis of the findings noted below. Firstly, solvent engineering and preliminary data are covered, which is then followed by data collected through the different characterization steps, namely XRD and GIWAXS. The solvent mixture is then discussed, then the PL results are analyzed. And finally, the device data is covered along with stability results. The information included in chapter 4 is an expanded version of the work published as a research article in the Advanced Photonics Research Journal on the 23rd of August, 2022.

4.1 PRELIMINARY WORK

The bulk of the experiments in this project were done to create and characterize perovskite films made using 3.0M precursor solutions with DMSO, GBL, and NMP in 1:1 and 1:0 mix ratios. There were also experiments with DMF solutions and mixtures of other ratios which were not completed with all solvents. These experiments were primarily evaluated with optical microscopy, with XRD also performed on some films.

Preliminary work with DMF precursor solutions found that a 0.13M ratio was less prone to failure and produced some large crystals which can be seen in the transmission light microscope images of Figure 26, although the films contain gaps similar to unfavourable wire-like microstructures common at higher molarity.

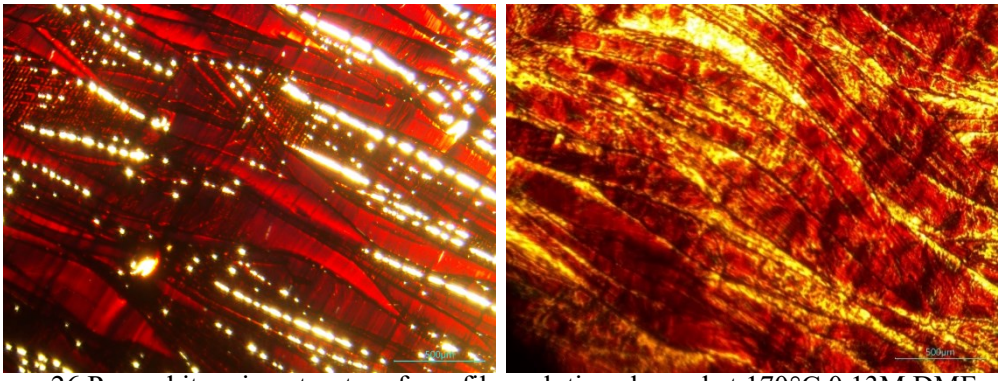

Figure 26 Perovskite microstructure from film solution sheared at 170°C 0.13M DMF precursor (left) and 0.13M 1:4 DMF:DMSO (right)

The largest crystals without gaps from DMF containing precursors came from mixtures of DMF and DMSO. Solutions with a 1:1 ratio of DMF and DMSO produced films with similar coverage issues to those of pure DMF solutions. The 1:3 and 1:4 ratios of the solvents produced films with good coverage and large crystals, but they suffered from degradation as seen in Figure 26.

Solutions of DMF with NMP or GBL proved to be very difficult to work with, creating incomplete films with poor coverage at multiple ratios. The continued issues and inability to make a full comparison across all solvent mixtures caused DMF to be discontinued in this project.

At the time DMF work was discontinued, so was work on mixtures other than a 1:1 ratio. This reduction in scope was primarily due to time constraints. The preliminary work with these other mixtures produced some films with large crystals and interesting morphologies, notable the DMSO and NMP mixtures seen below in the transmission light microscope images of Figure 27.

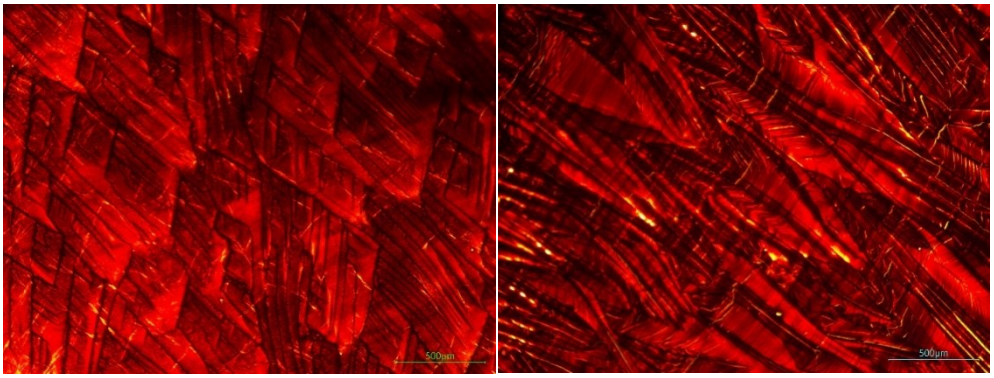

Figure 27 Perovskite films from 1:3 DMSO NMP mixtures sheared at 180 °C and 170 °C

4.2 SOLVENT ENGINEERING

The MAPbI3 crystallization process in solution sheared coated films originating from precursors dissolved in three solvents, DMSO, GBL and NMP, were evaluated. All solvents produced repeatable conformal films. Figure 28 depicts the top view surface morphology of the different samples.

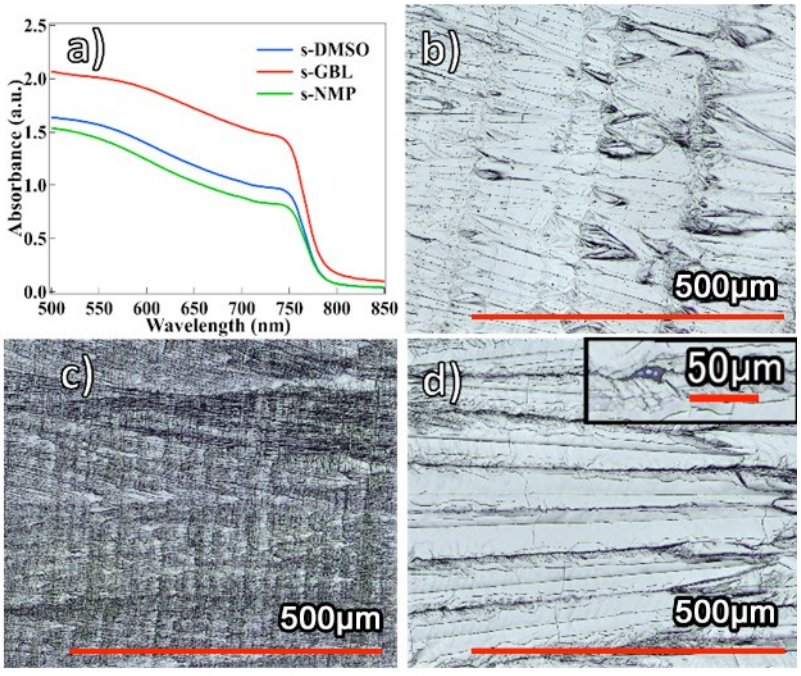

Figure 28 a) Absorbance spectroscopy of high temperature solution sheared perovskite films produced from DMSO, GBL, and NMP solutions; SEM Microstructure images of the same samples: b) s-DMSO, c) s-GBL, and d) s-NMP

Temperatures were adjusted during deposition to be near the solvents' boiling points (~10-30°C below). Temperatures were avoided if they were at or above the boiling point that led to visibly burned films, and crystalline films were produced across all samples covering a one inch by one inch glass substrate (refer to Methods). We adjusted the deposition conditions to produce consistent average film thicknesses of 1.3 μm for all samples. Increasing speeds and lowering temperatures reduced thickness but not all precursor solutions could produce consistent films under any set of conditions. Thin films sheared from GBL (s-GBL) were a challenge, while thicker films achieved uniform coverage. This translated to a higher absorption profile in films for s-GBL, which were especially noticeable in their UV-Visible absorption spectrum seen in Figure 28a.

The choice of solvent had a significantly greater effect on film morphology in crystal growth, direction, and size difference than previously reported in solution shearing. Typically, the solution shearing process imparts a directionality onto the films, and crystals grow in a preferred orientation along the blade's direction, which is consistent with other blade coating work. It was observed that GBL dispersed solutions produce much finer MAPbI3 crystals compared to DMSO and NMP as depicted in Figure 28b-d. Furthermore, as seen in Figure 28c, s-GBL samples display frequent and unexpected ridges perpendicular to the movement of the blade, caused by fast crystallization occurring close to the blade edge. S-GBL crystallizes quickly as the solubility of all precursor ingredients in GBL are shown to be inferior to that in other solvents[61], and an inverse temperature solubility phenomenon is observed with GBL perovskite solutions[69]. Therefore, the high temperature of the solution shearing deposition process promotes excess nucleation sites and fast crystallization in sheared films made from GBL compared to those from DMSO and NMP, which delay the crystallization of perovskite. A low number of nucleation sites (fast nucleation) and slow crystallization typically produces larger MAPbI3 crystals[16,70]. However, we note that stresses in the large crystals of both films produced from DMSO and NMP solutions shown in Figure 28 appear to have fracture lines within them, which cause poor stability because degradation mainly occurs at grain boundaries.

Sheared films from NMP solution (s-NMP) solvent contain consistently wider crystals than those in the sheared films made from DMSO (s-DMSO). However, gaps that occurred along their grain boundaries pose a major challenge toward using them to make efficient optoelectronic devices. S-NMP films were consistently deposited without pinholes, but those films were prone to short fissures that ran along the edges of crystals which penetrated the full thickness of the film highlighted in Figure 28d. A compositional analysis would provide analytical information on the crystal growth process of $MAPbI_3$ used in solution shearing coatings. Therefore, X-ray diffraction was used to quantify the crystalline properties of the films.

4.3 XRD RESULTS

XRD results, shown in Figure 29, show that all films correspond to the tetragonal perovskite phase, with some additional peaks seen in the s-DMSO films and s-NMP films. The peaks below a 2θ of 10° correspond to solvent intermediate phases identified as MAI-PbI_2-DMSO and MAI-PbI_2-NMP. The s-DMSO had small intermediate peaks suggesting a negligible amount of this phase in the film, unlike the s-NMP, which appears to have a larger number of intermediates as demonstrated by the large peak at 8.2°. These intermediates are observed in perovskite films produced at low temperatures and are thought to help with crystal formation by slowing the formation of the perovskite phase, which reduces defects and improves electrical performance of the resulting devices. The peaks associated with intermediate phases are inherently stable at room temperature and were removable by annealing at temperatures greater than 100°C for less than 20 minutes[71]. However, we did not observe the disappearance of these peaks or their intermediate phases in either the s-DMSO and s-NMP films after annealing at 100°C for over 20 minutes, which disagrees with published reports when using these solvents to form spin coated film. It was hypothesized that flash heating using temperatures over 150°C for the short solution shearing duration traps the phases and does not enable the full perovskite transition.

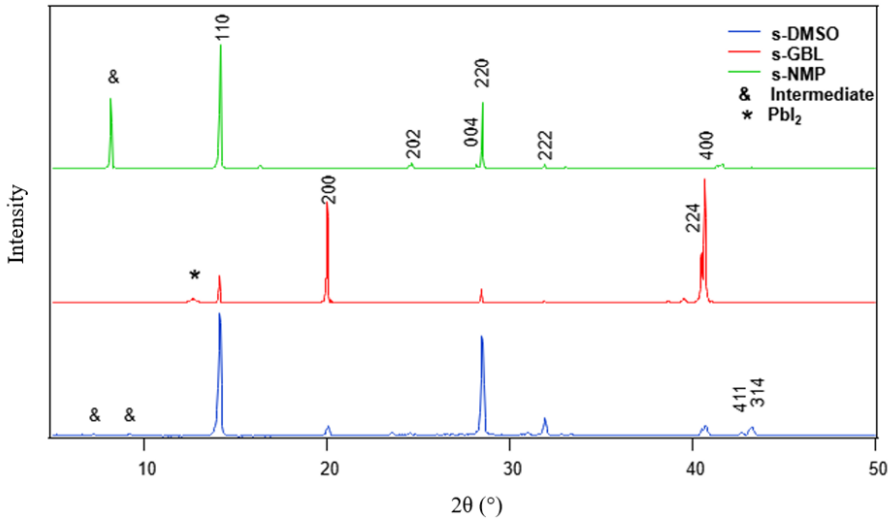

Figure 29 X-ray diffractogram of high temperature solution sheared perovskite films produced from DMSO, GBL, and NMP solutions

Several parameters were adjusted to determine if the presence of these intermediates was the product of a single processing condition. To test this, films were annealed for longer and at higher temperatures. S-NMP films were then annealed at temperatures up to 110°C for 8 hours without observing a notable reduction in the respective intermediate peak size. The NMP intermediate peak persisted for all the solution shearing conditions that were tested, including shearing temperatures as high as 200°C. Unlike the other films studied in this work, the s-GBL did not show any XRD signatures of intermediates. MAI-PbI_2-GBL intermediate peaks would be at 5.37°, 8.22° and 10.79°, which are clearly absent in the film. The films did show signs of unreacted precursor ingredients however, as suggested by the PbI_2 peak at 12.7°.

The $MAPbI_3$ film solution sheared from DMSO shows a strong (110) peak; however, the $MAPbI_3$ films solution sheared from DMSO originally reported by Koleilat research group in 2019 work show strong (200) peaks in agreement with other solution shearing reports. Ferroelasticity, or the presence of subgrain twin domains of differing orientation like the (110)/(200) planes present here, are inherent in tetragonal $MAPbI_3$ perovskite films [72]. Kennard et al. used GIWAXS to show that the {110} and {200} families of planes are the predominant twin domain types in $MAPbI_3$ [73]. At room temperature, $MAPbI_3$ perovskite films possess ferroelastic domains that cohabitate the same crystal grain because of the

phase transition that the material goes through after synthesis. Above 100 °C, the perovskite crystal phase adopts a cubic structure, and as it cools it experiences a structural phase transition around 57 °C to adopt a tetragonal structure, which is stable at room temperature. The phase transition leads to different possibilities for the orientation of the tetragonal axis, leading to the formation of twin domains. The twin domains nucleate point defects and facilitate ion diffusion. The more twin domain walls the greater the degradation because there will be more crystal vacancies and defects and more ion diffusion. The s-GBL showed a dominant, consistent (200) peak rather than the (110) peak; however, the (110) peak remains. It is believed both twin domain orientations exist in part in all the solution sheared films; while the (110) peak is most widely reported with spin coated films, solution sheared films contain both the {110} and the {200} orientations to varying degrees. Specifically, GBL films preferentially display the (200) peak and more twinning, as seen in Figure 29. The strong focus on the (200) orientation may be unique to this deposition method.

4.4 GIWAXS PATTERNS

To clarify the crystallographic properties of our solution sheared films, GIWAXS patterns are presented in Figure 30. All sheared samples feature the (110) and (220) lattice planes at q = 1.0 $Å^{-1}$ and 2.0 $Å^{-1}$ characteristic of crystalline $MAPbI_3$ perovskite, as well as the (200) peak to varying degrees [49,74,75]. In general, the homogeneous spread in the intensities and the blunt Bragg spots featured in the spin coated sample (Figure 30a) points to a low degree of preferential crystallographic orientation. All solution sheared samples demonstrate more preferential crystallographic orientation than the spin coated sample. The s-DMSO sample and the s-NMP sample both display preferential crystallographic orientation over the s-GBL sample. The sharper diffraction intensity concentrated into thin arc segments is characteristic of textured crystals rather than the full semi-circle widely reported in isotropic 3D $MAPbI_3$ perovskite crystallization. The s-GBL samples feature longer arc segments and more isotropic crystals, possibly resulting from the degradation from ion diffusion resulting from the grain boundaries or more pronounced twin domains. The GBL sample expresses an arc for the (200) peak, though it does not appear intense or highly ordered as expected from the XRD in Figure 29. The GBL sample for GIWAXS was made

at 10 °C higher temperature than the sample for XRD. While XRD was taken right after sample fabrication, GIWAXS samples were taken several days after sample preparation. It could be that the higher temperature or the high intensity X-ray beam (15.1 keV) caused chemical stress that moved the domain walls of the GBL samples and switched the twin domain orientation. The GBL sample is indicative of more random isotropic orientations as opposed to preferred orientations. This result could also be due to the fast degradation and general instability of the s-GBL samples compared to the other samples because decomposition reduces overall intensity and broadens perovskite Bragg peaks. On the other hand, s-NMP samples showcased smaller, sharper points, denoting a higher degree of crystallinity and order than all others, which indicates that NMP inclusion benefits perovskite device fabrication.

The s-NMP and s-DMSO films have small arcs near the center of Figures 30b and 30d that correlate to the intermediate compounds seen in the XRD, which show a highly crystalline phase within the samples. The spot that corresponds to the s-NMP intermediate has such a large intensity in the GIWAXS shown in Figure 30d that it nearly overshadowed the short (110) arc. This is further indication of the retention of the intermediate phase after annealing.

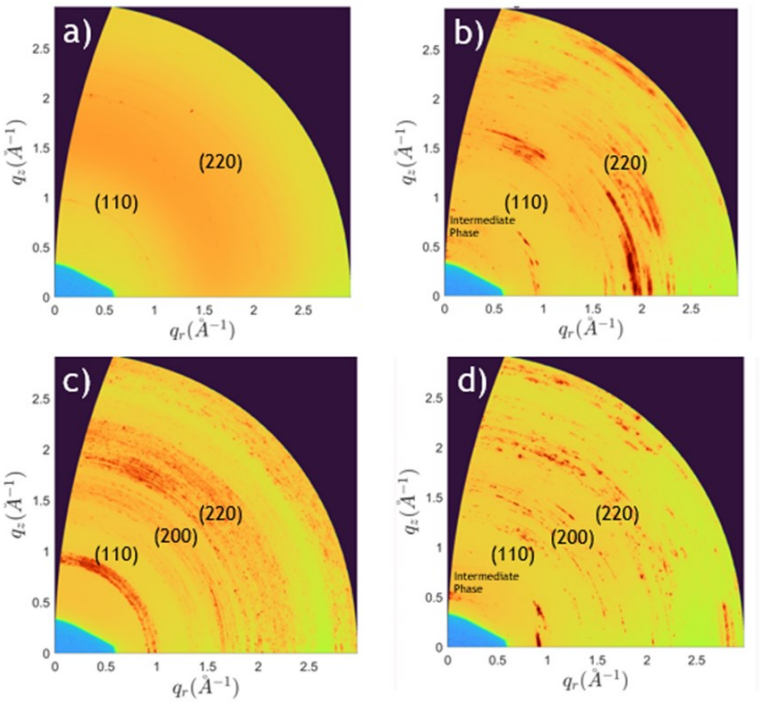

Figure 30 GIWAXS patterns of a) room temperature spin-coated perovskite film produced from a DMSO solution. GIWAXS patterns from high temperature solution sheared films produced from b) DMSO, c) GBL, and d) NMP solutions. The incidence angle for GIWAXS is 0.15°

4.5 SOLVENT MIXTURES

Each solvent uniquely affects crystal growth so to further understand this, mixed solvent MAPbI3 solution sheared films were fabricated. Three films were created from binary combinations of equal volume fractions of each solvent. To avoid confusion, the sheared films will be referred to as follows: the s-DN films are the ones formed from a mixture of DMSO and NMP, the s-DG films are the ones formed from a mixture of DMSO and GBL, and the s-GN films are the ones made from a mixture of GBL and NMP. As depicted in Figure 31, the morphology of the mixed solvent films has features that are distinct from films made with their individual component solvents. None of the samples showed crystal fractures throughout the thickness of the films as seen in some samples made from pure solvents, and the crystals appear bigger in the films prepared from binary mixtures. The s-DG films, shown in Figure 31b, have large grains with raised sections at the edges along with sparse dendritic features. The lines that run across the width of the crystal create rough

regions, which can be clearly seen in Figure 31b. Many areas on the surface of the crystals show signs of degradation (yellowing colour seen on the crystal faces and near edges and defects caused by degradation to PbI_2) suggesting that this solvent mixture produced unstable films, compared to the other samples.

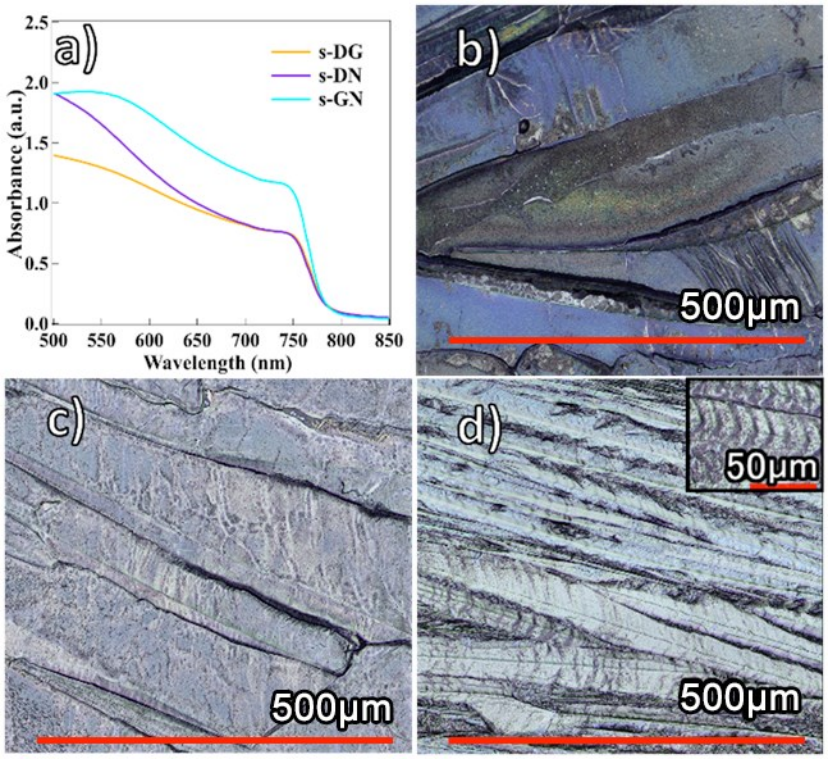

Figure 31 a) Absorbance spectroscopy of high temperature solution sheared perovskite films produced from mixed solvent solutions with a (1:1) ratio. Microstructure images of the same samples: b) s-DG (DMSO:GBL), c) s-DN (DMSO:NMP), and d) s-GN (GBL:NMP)

The s-DN films were visually comparable to s-DG as they contained large crystals but did not show the significant ridges within their crystal domains that s-DG possessed. They were also the smoothest films with an average roughness of around 600 nm, a reduction of 40% from the initial films. Additionally, the signs of degradation present in the s-DG films were not present in these films.

The s-GN film resembled the film made purely from NMP although the edges of the long thin crystals appear rough. There are chevron patterns on the surface of the crystals, possibly caused by the continued growth of the dendrites that formed them. This growth

pattern has been observed on other perovskite films and can be seen forming the figure below. It is suspected that this growth increased grain boundaries and would be highly detrimental for devices, because grain boundaries negatively affect carrier mobility and lifetime[76].

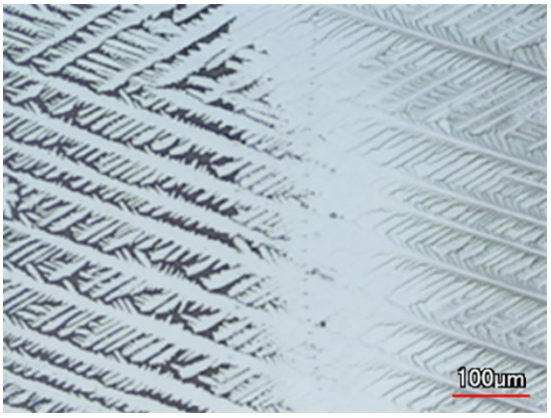

Figure 32 Microstructure of dendritic growth in perovskite sample

The signs of degradation in the s-DG that are visually observed in Figure 31b can also be observed in the GIWAXS pattern in Figure 33a. Signs of this degradation are noted by the PbI2 peak that appears at qz = 0.9 Å-1. Intermediate peaks for both NMP and DMSO are seen in the s-DN sample pattern along with the expected tetragonal perovskite phase. While all mixed solvent samples show a high degree of crystallinity in the GIWAXS patterns, Figure 33b and Figure 33c contain sharp Bragg points indicative of highly ordered crystals (circled in Figure 33b). These spots are indicative of extreme order, usually reserved to 2D perovskite structures. The shearing process, along with the high coordination of DMSO and NMP with MAPbI3 precursors and the mixtures' different evaporation rates resulted in reduced nucleation sites and slowed crystal growth allowing for expansion of existing crystal domains, resulting in much larger crystals with more preferred orientation.

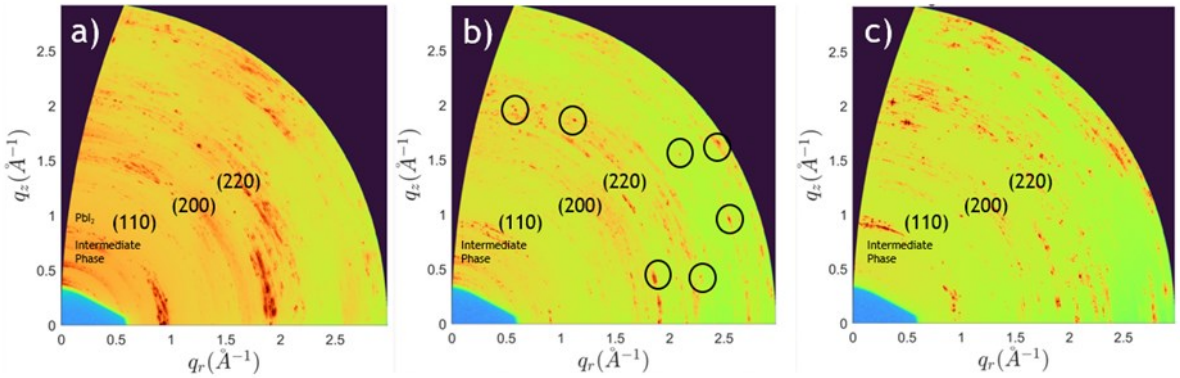

Figure 33 GIWAXS patterns from high temperature solution sheared films produced from mixed solvent solutions with a (1:1) ratio: a) s-DG (DMSO:GBL), b) s-DN (DMSO:NMP), and c) s-GN (GBL:NMP). The incidence angle for GIWAXS is 0.15°.

4.6 PHOTOLUMINESCENCE RESULTS

We proceeded to analyze the potential of the solution sheared $MAPbI_3$ films deposited from various solvent mixtures in optoelectronic applications. For that purpose, we measured their photoluminescence. Radiative recombination may not be desired in a device application but will occur in this closed system and at a slower rate than trap-assisted recombination. Trap-assisted non-radiative recombination quenches the PL intensity, therefore better crystallinity is associated with higher PL intensity[77].

Figure 34 summarizes the PL performance of all the samples presented in this work. All exhibited a secondary peak or shoulder at 795 nm. However, it was observed that these secondary peaks are approximately the same size regardless of solvent mixtures used in this study. This secondary peak is caused by reflected and reabsorbed light, which is emitted at a lower energy[44,78,79].

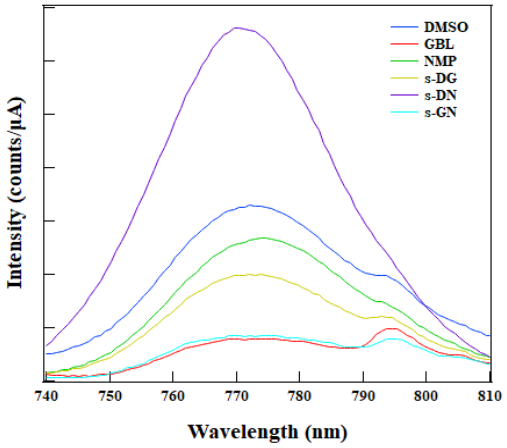

Figure 34 Photoluminescence spectrum of high temperature solution sheared perovskite films produced from pure and mixed solvent solutions.

The defects that allow for unfavourable non-radiative recombination are most common at grain boundaries. It is expected that samples made purely of GBL would have the weakest PL response as the smaller grains of the GBL crystals, with their chevron patterning, have a higher density of grain boundaries and thus higher defect density[21]. Films originating purely from GBL presented a low PL intensity consistent with dominant trap assisted recombination. It also appears the addition of GBL to the precursors reduces the quality of the resulting films, with s-GBL, s-GN and s-DG having the weakest PL responses. The s-DMSO and s-NMP films performed well in PL testing with similar results considering their absorption (refer to Figure 28). The s-DN film had the lowest absorption at the excitation wavelength of 670 nm (refer to Figure 31) of all samples and had PL responses above its pure solvent counterparts. This means a reduction in unfavourable recombination. This along with s-DN crystal size, lack of deformities within the film, and highly preferential orientation shown in the GIWAXS pattern, makes it a promising candidate for device applications.

After PL testing the same equipment was used to obtain before absorbance measurements on all perovskite films. From this test a Tauc plot was created to confirm the expected bandgap of the $MAPbI_3$ films which can be seen below in Figure 35. The band gap was approximated to 1.59eV which is in line with reported and calculated values for $MAPbI_3$ [80-82].

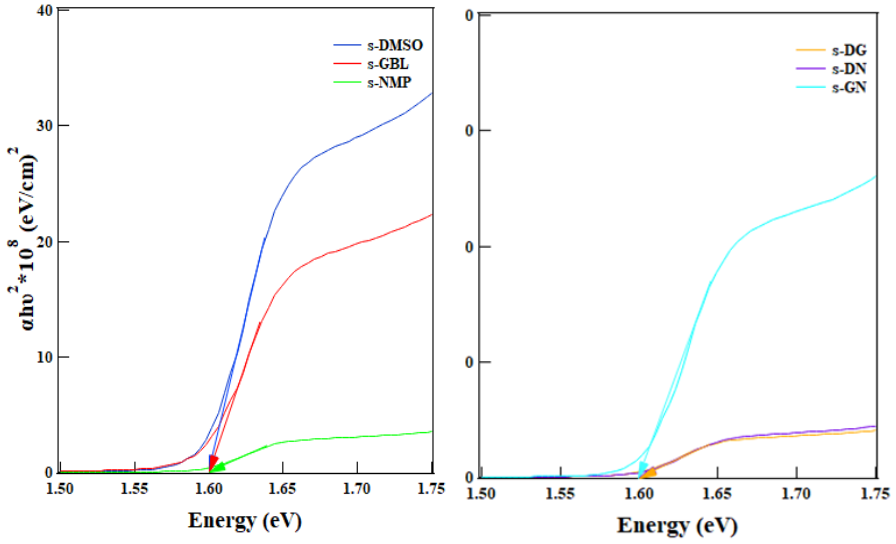

Figure 35 Tauc plots of absorbance data of high temperature solution sheared perovskite films produced from pure solvents DMSO, GBL, and NMP solutions on the left and from mixed solvent solutions with a (1:1) ratio: s-DG (DMSO:GBL), s-DN (DMSO:NMP), and s-GN (GBL:NMP) on the right.

4.7 SOLAR DEVICES STABILITY

Perovskite solar cells were created using the DMSO and NMP mixture to test its stability. The cells were produced on an indium tin oxide (ITO) glass substrate. The tin oxide (SnO_2) electron transport layer (ETL) was deposited using spin coating, while the perovskite absorbing layer and spiro-MeOTAD hole transport layer (HTL) used the same deposition method, either solution shearing or spin coating. Thermal evaporation was used to deposit gold contacts. The construction of a sheared solar cell can be seen in Figure 36. The perovskite crystal forms a consistent layer with a visibly rough surface. This surface roughness is exaggerated by the inconsistent thickness of the HTL.

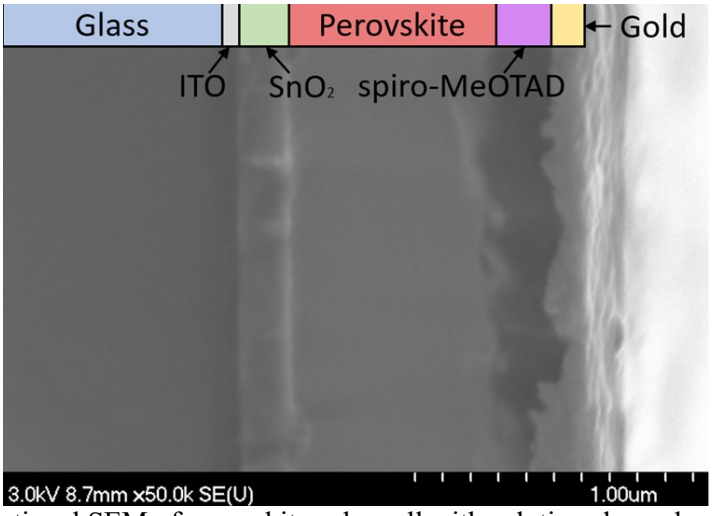

Figure 36 Cross-sectional SEM of perovskite solar cell with solution sheared perovskite and spiro-MeOTAD layers

All devices were tested under the solar simulator to compare their PCE. Each device had contacts deposited for eight "pixel" solar cells for testing. The third sheared cell and first spin coated cell underperformed across most pixels, likely due to processing inconsistencies. The sheared cells had on average better performance; the second sheared cell was chosen as the "champion" device for stability testing. Two of the pixels in the bottom corners of this device gave responses much lower than the others. This was believed to be caused by flaws in the contacts of the protype testing apparatus, which were not perfectly level and prone to making poor contact if unbalanced. Removing these two pixels, the device had an average normalized PCE of 95%, the highest of all the devices.

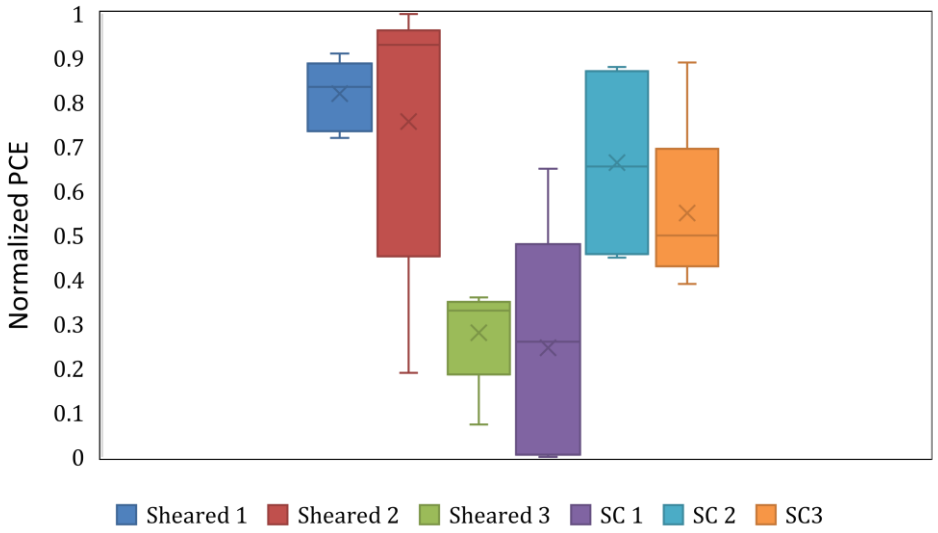

Figure 37 Normalized PCE of sheared and spin coated solar cells

The champion device was tested over the course of two weeks to determine its stability by taking JV measurements which were used to calculate the PCE of the solar cell. Photocurrent is used to track stability and the measurements normalized to the initial test are shown in Figure 37. The photocurrent stability of the device lends further credence to the stability of the intermediate phase observed in the s-DN films. Furthermore, the large grain size present in the s-DN film results in less grain boundaries and hence less degradation leading to enhanced stability.

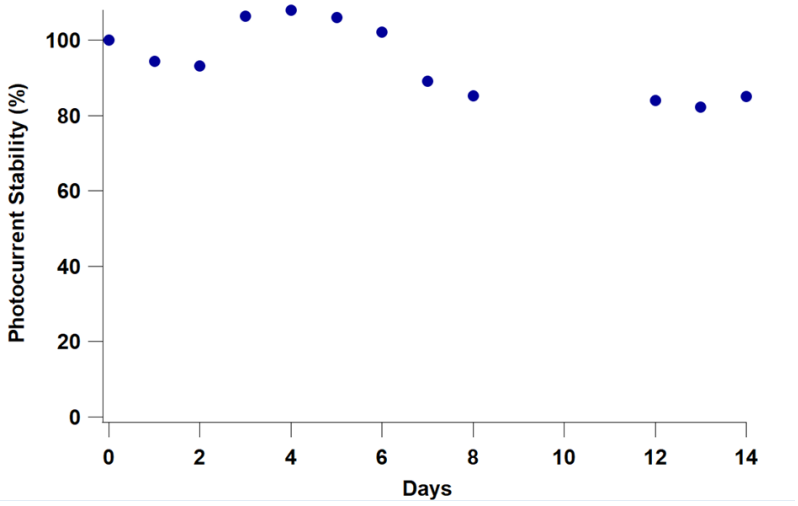

Figure 38 Normalized photocurrent of solution sheared perovskite solar cell stored in an N_2-filled glovebox.

4.8 CONCLUSION

Chapter 4 contains the specific results of the work done for the thesis, covering the chemistry conducted and the accompanying characterizations. The champion condition is then employed in a solar cell device where the stability data is collected over the course of two weeks and reported. The following chapter will conclude the work completed for this thesis.

CHAPTER 5 CONCLUSION

This chapter provides a list of conclusions to the discussion and speculates on the outlook for future work. This section also includes a brief list of other work and accomplishments the author conducted from the duration of time in the Koleilat lab.

5.1 RESEARCH CONCLUSIONS

- Solution sheared samples feature a new textured crystallographic orientation for 3D perovskite films owing to the deposition process and solvents.

- This work contained some of the Koleilat groups earliest work with the Canadian Light Source and GIWAXS analysis. Of the pure solvent mixtures, the films fabricated with DMSO and NMP feature the sharpest Bragg spots in their GIWAXS pattern. The s-DN and s-GN GIWAXS patterns show crystallographic orientation that demonstrates highly oriented traits. These results supplemented the other characterizations in the project and provided lessons on use of the technique that improved future and current work.

- GBL was initially of interest as being a greener alternative to other high temperature solvents but it was found to be a poor fit for the processing methods used. GBL-based crystals showed the poorest morphology and weakest PL response supporting the presence of deformities in the films.

- DMSO, GBL and NMP solvents were tested to determine if pure or (1:1) solvent mixtures yielded the most promising sheared perovskite films. DMSO when combined with NMP in a 1:1 ratio yielded PL results that are almost double the response obtained using pure DMSO.

- The perovskite solar cell created with a solvent mixture of DMSO and NMP showed excellent stability. Utilizing a combination of DMSO and NMP for lead halide perovskite precursor solutions is a promising avenue for future optoelectronics work.

- Future work should include exploration of mixing ratios of NMP and DMSO that were not completed in this project. Additional characterization methods should be used to validate the high performance of these pictures, such as TRPL (time resolved photoluminescence) and expanded solar cell testing.

- Furthermore, the lessons learned from the mixed solvent engineering of this project may be applied in combination with the other avenues of perovskite research in the Koleilat lab such as dimensional engineering and solvent post treatment.

5.2 OTHER WORK

During the time in the Koleilat lab other notable contributions were:

- Served as Lab manager and Safety officer for the Koleilat Lab maintaining glove boxes and key equipment throughout the pandemic.

- Supervised junior lab members and conducted lab training for new graduate students.

- Designed and installed upgrades for the shearing station with the help of department machinist Dean Grijm.

- Completed an industry affiliated project with Graphite Innovation and Technologies.

- Earned the following scholarships: Nova Scotia University Student, The Pengrowth Innovation Grant, The Bruce and Dorothy Rosetti Engineering Research Scholarship

- Authored and contributed to the following articles: Textured MAPbI3 Thin Films Achieved via Solvent Engineering in the Solution-Shearing Process (Benjamin T. Smith), Dimensionality engineering of metal halide perovskites (Rashad F. Kahwag)

- Attended the NSERC CREATE for Leaders in Energy Sustainability program and used the LES internship program to obtained work with Efficiency Nova Scotia.

BIBLIOGRAPHY

[1] G. B. Adugna, Y. T. Tao, *J. Chinese Chem. Soc.* **2023**, 1.

[2] H. S. Lee, M. K. Kim, S. R. Pae, D. Kim, H. J. Seo, P. Boonmongkolras, I. Gereige, S. Park, B. Shin, *Nano Energy* **2020**, *74*, 104830.

[3] Z. Chen, B. Turedi, A. Y. Alsalloum, C. Yang, X. Zheng, I. Gereige, A. Alsaggaf, O. F. Mohammed, O. M. Bakr, *ACS Energy Lett.* **2019**, *4*, 1258.

[4] A. Y. Alsalloum, B. Turedi, X. Zheng, S. Mitra, A. A. Zhumekenov, K. J. Lee, P. Maity, I. Gereige, A. AlSaggaf, I. S. Roqan, O. F. Mohammed, O. M. Bakr, *ACS Energy Lett.* **2020**, *5*, 657.

[5] X. Li, P. Xie, X. Mo, Y. Xiang, Z. Xiao, T. Xiongsong, H. Huang, J. Sun, G. Dai, J. Yang, *Phys. Status Solidi - Rapid Res. Lett.* **2020**, DOI 10.1002/pssr.202000479.

[6] Y. Li, Y. Zhang, T. Li, X. Tang, M. Li, Z. Chen, Q. Li, Q. Sheng, W. Shi, J. Yao, *J. Mater. Chem. C* **2020**, *8*, 12148.

[7] C. Xie, C. K. Liu, H. L. Loi, F. Yan, *Adv. Funct. Mater.* **2020**, *30*, 1.

[8] H. Do Kim, S. V. N. Pammi, H. W. Lee, S. W. Lee, S. G. Yoon, J. Park, Y. J. Kim, H. S. Kim, *J. Alloys Compd.* **2020**, *815*, 152404.

[9] Z. Ouyang, H. Abrams, R. Bergstone, Q. Li, F. Zhu, D. Li, *Adv. Energy Mater.* **2020**, *10*, 1.

[10] L. Zhao, K. M. Lee, K. Roh, S. U. Z. Khan, B. P. Rand, *Adv. Mater.* **2019**, *31*, 1.

[11] R. F. Kahwagi, S. T. Thornton, B. Smith, G. I. Koleilat, *Front. Optoelectron.* **2020**, *13*, 196.

[12] K. T. Munson, E. R. Kennehan, G. S. Doucette, J. B. Asbury, *Chem* **2018**, *4*, 2826.

[13] H. Li, C. Zuo, A. D. Scully, D. Angmo, J. Yang, M. Gao, *Flex. Print. Electron.* **2020**, *5*, DOI 10.1088/2058-8585/ab639e.

[14] R. Wang, M. Mujahid, Y. Duan, Z. K. Wang, J. Xue, Y. Yang, *Adv. Funct. Mater.* **2019**, *29*, 1.

[15] F. Guo, S. Qiu, J. Hu, H. Wang, B. Cai, J. Li, X. Yuan, X. Liu, K. Forberich, C. J. Brabec, Y. Mai, *Adv. Sci.* **2019**, *6*, DOI 10.1002/advs.201901067.

[16] M. Jung, S. G. Ji, G. Kim, S. Il Seok, *Chem. Soc. Rev.* **2019**, *48*, 2011.

[17] P. H. Huang, Y. H. Wang, J. C. Ke, C. J. Huang, *Energies* **2017**, *10*, 1.

[18] W. Y. Tan, P. P. Cheng, Y. W. Zhang, J. M. Liang, X. Chen, Y. Liu, Y. Min, *J. Mater. Chem. C* **2019**, *7*, 6004.

[19] N. Chen, D. H. Kim, P. Kovacik, H. Sojoudi, M. Wang, K. K. Gleason, *Annu. Rev.*

Chem. Biomol. Eng. **2016**, *7*, 373.

[20] Y. Zhao, J. Wei, H. Li, Y. Yan, W. Zhou, D. Yu, Q. Zhao, *Nat. Commun.* **2016**, *7*, 1.

[21] W. Nie, J. C. Blancon, A. J. Neukirch, K. Appavoo, H. Tsai, M. Chhowalla, M. A. Alam, M. Y. Sfeir, C. Katan, J. Even, S. Tretiak, J. J. Crochet, G. Gupta, A. D. Mohite, *Nat. Commun.* **2016**, *7*, 1.

[22] NREL, *Natl. Renew. Energy Lab.* **2019**, 1.

[23] Y. H. Kim, C. Wolf, H. Kim, T. W. Lee, *Nano Energy* **2018**, *52*, 329.

[24] M. Baranowski, P. Plochocka, *Adv. Energy Mater.* **2020**, *1903659*, DOI 10.1002/aenm.201903659.

[25] Y. Li, D. Song, J. Meng, J. Dong, Y. Lu, X. Huo, A. Maqsood, Y. Song, S. Zhao, B. Qiao, Z. Xu, *J. Mater. Sci.* **2020**, *55*, 9787.

[26] J. Chen, Y. Xiong, Y. Rong, A. Mei, Y. Sheng, P. Jiang, Y. Hu, X. Li, H. Han, *Nano Energy* **2016**, *27*, 130.

[27] E. Radicchi, A. Kachmar, E. Mosconi, B. Bizzarri, F. Nunzi, F. De Angelis, *J. Phys. Chem. Lett.* **2020**, *11*, 6139.

[28] C. M. Tsai, G. W. Wu, S. Narra, H. M. Chang, N. Mohanta, H. P. Wu, C. L. Wang, E. W. G. Diau, *J. Mater. Chem. A* **2017**, *5*, 739.

[29] J. Chen, N. G. Park, *Adv. Mater.* **2019**, *31*, 1.

[30] X. Cao, L. Zhi, Y. Jia, Y. Li, K. Zhao, X. Cui, L. Ci, D. Zhuang, J. Wei, *ACS Appl. Mater. Interfaces* **2019**, *11*, 7639.

[31] N. G. Park, K. Zhu, *Nat. Rev. Mater.* **2020**, *5*, 333.

[32] L. Zhi, Y. Li, X. Cao, Y. Li, X. Cui, L. Ci, J. Wei, *J. Energy Chem.* **2019**, *30*, 78.

[33] R. Swartwout, M. T. Hoerantner, V. Bulović, *Energy Environ. Mater.* **2019**, *2*, 119.

[34] Z. Li, T. R. Klein, D. H. Kim, M. Yang, J. J. Berry, M. F. A. M. Van Hest, K. Zhu, *Nat. Rev. Mater.* **2018**, *3*, 1.

[35] M. M. Hasan, C. Clegg, M. Manning, A. El Ghanam, C. Su, M. D. Harding, C. Bennett, I. G. Hill, G. I. Koleilat, *ACS Photonics* **2020**, *7*, 57.

[36] M. M. Hasan, C. Clegg, M. Manning, A. El Ghanam, C. Su, M. D. Harding, C. Bennett, I. G. Hill, G. I. Koleilat, *ACS Photonics* **2020**, *7*, 57.

[37] M. K. Kim, H. S. Lee, S. R. Pae, D. J. Kim, J. Y. Lee, I. Gereige, S. Park, B. Shin, *J. Mater. Chem. A* **2018**, *6*, 24911.

[38] J. Li, Y. Liu, X. Ren, Z. Yang, R. Li, H. Su, X. Yang, J. Xu, H. Xu, J. Y. Hu, A. Amassian, K. Zhao, S. F. Liu, *Adv. Opt. Mater.* **2017**, *5*, 1.

[39] Y. Wu, A. Islam, X. Yang, C. Qin, J. Liu, K. Zhang, W. Peng, L. Han, *Energy Environ. Sci.* **2014**, *7*, 2934.

[40] N. K. Noel, S. N. Habisreutinger, B. Wenger, M. T. Klug, M. T. Hörantner, M. B. Johnston, R. J. Nicholas, D. T. Moore, H. J. Snaith, *Energy Environ. Sci.* **2017**, *10*, 145.

[41] C. Jacoboni, *Semiconductors*, **2010**.

[42] M. O. Forgacs D, Wojciechowski K, *Perovskite Photovoltaics: From Laboratory to Industry*, Springer Berlin Heidelberg, **2020**.

[43] D. Meggiolaro, S. G. Motti, E. Mosconi, A. J. Barker, J. Ball, A. Riccardo, F. Deschler, A. Petrozza, F. De Angelis, *Energy Environ. Sci.* **2018**, *11*, 702.

[44] L. M. Herz, *Annu. Rev. Phys. Chem.* **2016**, *67*, 65.

[45] G. Xing, B. Wu, X. Wu, M. Li, B. Du, Q. Wei, J. Guo, E. K. L. Yeow, T. C. Sum, W. Huang, *Nat. Commun.* **2017**, *8*, DOI 10.1038/ncomms14558.

[46] W. Nie, H. Tsai, R. Asadpour, A. J. Neukirch, G. Gupta, J. J. Crochet, M. Chhowalla, S. Tretiak, M. A. Alam, H. Wang, **2015**, *347*, 522.

[47] H. Jin, E. Debroye, M. Keshavarz, I. G. Scheblykin, M. B. J. Roeffaers, J. Hofkens, J. A. Steele, *Mater. Horizons* **2020**, *7*, 397.

[48] S. D. Stranks, G. E. Eperon, G. Grancini, C. Menelaou, M. J. P. Alcocer, T. Leijtens, L. M. Herz, A. Petrozza, H. J. Snaith, **2013**, *342*, 341.

[49] H. Ren, S. Yu, L. Chao, Y. Xia, Y. Sun, S. Zuo, F. Li, T. Niu, Y. Yang, H. Ju, B. Li, H. Du, X. Gao, J. Zhang, J. Wang, L. Zhang, Y. Chen, W. Huang, *Nat. Photonics* **2020**, *14*, 154.

[50] D. J. Freppon, L. Men, S. J. Burkhow, J. W. Petrich, J. Vela, E. A. Smith, *J. Mater. Chem. C* **2017**, *5*, 118.

[51] C. Reichardt, T. Welton, *Solvents Solvent Eff. Org. Chem. Fourth Ed.* **2010**, DOI 10.1002/9783527632220.

[52] Y. Deng, Q. Wang, Y. Yuan, J. Huang, *Mater. Horizons* **2015**, *2*, 578.

[53] N. Ahn, D. Y. Son, I. H. Jang, S. M. Kang, M. Choi, N. G. Park, *J. Am. Chem. Soc.* **2015**, *137*, 8696.

[54] M. I. Saidaminov, A. L. Abdelhady, G. Maculan, O. M. Bakr, *Chem. Commun.* **2015**, *51*, 17658.

[55] X. Li, Y. Chen, L. Li, J. Huang, *Materials (Basel).* **2018**, *11*, DOI 10.3390/ma11091759.

[56] H. Mehdi, A. Mhamdi, A. Bouazizi, *Mater. Sci. Semicond. Process.* **2020**, *109*, 104915.

[57] J. Li, R. Munir, Y. Fan, T. Niu, Y. Liu, Y. Zhong, Z. Yang, Y. Tian, B. Liu, J. Sun,

D. M. Smilgies, S. Thoroddsen, A. Amassian, K. Zhao, S. (Frank) Liu, *Joule* **2018**, *2*, 1313.

[58] E. Radicchi, E. Mosconi, F. Elisei, F. Nunzi, F. De Angelis, *ACS Appl. Energy Mater.* **2019**, *2*, 3400.

[59] Z. Arain, C. Liu, Y. Ren, Y. Yang, M. Mateen, X. Liu, Y. Ding, Z. Ali, X. Liu, S. Dai, T. Hayat, A. Alsaedi, *ACS Appl. Mater. Interfaces* **2019**, *11*, 16704.

[60] J. Chen, Y. Xiong, Y. Rong, A. Mei, Y. Sheng, P. Jiang, Y. Hu, X. Li, H. Han, *Nano Energy* **2016**, *27*, 130.

[61] Y. Deng, C. H. van Brackle, X. Dai, J. Zhao, B. Chen, J. Huang, *Sci. Adv.* **2019**, *5*, 1.

[62] M. Yang, Z. Li, M. O. Reese, O. G. Reid, D. H. Kim, S. Siol, T. R. Klein, Y. Yan, J. J. Berry, M. F. A. M. Van Hest, K. Zhu, *Nat. Energy* **2017**, *2*, 1.

[63] W. L. Bragg, **1914**, 1922.

[64] "GISAXS - GISAXS," can be found under http://gisaxs.com/index.php/GISAXS, **n.d.**

[65] "G I S A X S," can be found under http://www.gisaxs.de/theory.html, **2018**.

[66] "Photoluminescence," **2011**.

[67] A. R. Srimath Kandada, C. Silva, *J. Phys. Chem. Lett.* **2020**, DOI 10.1021/acs.jpclett.9b02342.

[68] "Duetta-Fluorescence and Absorbance Spectrometer - HORIBA - HORIBA," can be found under https://www.horiba.com/int/scientific/products/detail/action/show/Product/duetta-1621/, **n.d.**

[69] Y. Jo, K. S. Oh, M. Kim, K. H. Kim, H. Lee, C. W. Lee, D. S. Kim, *Adv. Mater. Interfaces* **2016**, *3*, 1.

[70] F. Hao, C. C. Stoumpos, P. Guo, N. Zhou, T. J. Marks, R. P. H. Chang, M. G. Kanatzidis, *J. Am. Chem. Soc.* **2015**, *137*, 11445.

[71] Z. Jiang, *J. Appl. Crystallogr.* **2015**, *48*, 917.

[72] A. A. Medjahed, T. Zhou, J. Camilo, A. Quiceno, P. Dally, P. Pochet, T. U. Schülli, D. Djurado, P. Reiss, S. Pouget, **2022**, *2103627*, DOI 10.1002/aenm.202103627.

[73] R. M. Kennard, C. J. Dahlman, R. A. Decrescent, J. A. Schuller, K. Mukherjee, R. Seshadri, M. L. Chabinyc, **2021**, DOI 10.1021/acs.chemmater.0c03776.

[74] D. M. Delongchamp, R. J. Kline, D. A. Fischer, L. J. Richter, M. F. Toney, *Adv. Mater.* **2011**, *23*, 319.

[75] D. Hong, J. Li, S. Wan, I. G. Scheblykin, Y. Tian, *J. Phys. Chem. C* **2019**, *123*,

12521.

[76] K. Chen, S. Schu, **2018**, DOI 10.1039/c8cs00212f.

[77] P. Padhye, P. Poddar, *J. Mater. Chem. A Mater. energy Sustain.* **2014**, *2*, 19189.

[78] H. Diab, C. Arnold, F. Lédée, G. Trippé-Allard, G. Delport, C. Vilar, F. Bretenaker, J. Barjon, J. S. Lauret, E. Deleporte, D. Garrot, *J. Phys. Chem. Lett.* **2017**, *8*, 2977.

[79] K. Schötz, A. M. Askar, W. Peng, D. Seeberger, T. P. Gujar, M. Thelakkat, A. Köhler, S. Huettner, O. M. Bakr, K. Shankar, F. Panzer, *J. Mater. Chem. C* **2020**, *8*, 2289.

[80] P. Fan, D. Gu, G. X. Liang, J. T. Luo, J. L. Chen, Z. H. Zheng, D. P. Zhang, *Sci. Rep.* **2016**, *6*, 1.

[81] A. M. A. Leguy, P. Azarhoosh, M. I. Alonso, M. Campoy-Quiles, O. J. Weber, J. Yao, D. Bryant, M. T. Weller, J. Nelson, A. Walsh, M. Van Schilfgaarde, P. R. F. Barnes, *Nanoscale* **2016**, *8*, 6317.

[82] T. Baikie, Y. Fang, J. M. Kadro, M. Schreyer, F. Wei, S. G. Mhaisalkar, M. Graetzel, T. J. White, *J. Mater. Chem. A* **2013**, *1*, 5628.